Road Surface Characterization by Near-Infrared Light Scattering and Absorption

Alexander Permogorov

School of Electrical Engineering

Thesis submitted for examination for the degree of Master of Science in Technology.

Espoo October 10, 2016

Thesis supervisor:

Prof. Markku Sopanen

Thesis advisor:

D.Sc. (Tech.) Ari Tuononen

Aalto University
School of Electrical
Engineering

AALTO UNIVERSITY
SCHOOL OF ELECTRICAL ENGINEERING

ABSTRACT OF THE
MASTER'S THESIS

Author: Alexander Permogorov

Title: Road Surface Characterization by Near-Infrared Light Scattering and Absorption

Date: October 10, 2016 Language: English Number of pages: 5+51

Department of Micro- and Nanosciences

Professorship: S-104

Supervisor: Prof. Markku Sopanen

Advisor: D.Sc. (Tech.) Ari Tuononen

This work is dedicated to creation of a non-contact optical sensor for tire-road friction estimation based on near-infrared radiation scattering and absorption in the case of different road conditions. Here we present implementation of such a sensor based on different detector response to backscattered light from the asphalt surface in four possible conditions: dry, wet, snowy and icy. We discuss light-matter interaction behind the chosen methodology, describe such a sensor prototype and its optical and electric components, perform experimental evaluation of sensor's ability to distinguish these surface types and compare experimental results to computer simulations. Theory, experiment and simulations come in agreement and the road conditions can be determined with the sensor. Additionally, ideas of sensor improvement and further perspectives are discussed.

Keywords: near infrared, scattering, absorption, friction estimation, laser diode, photodiode

Preface

I want to thank Dr. Ari Tuononen for his great patience and guidance during my work in his department and valuable insight into fascinating area of vehicle engineering, Prof. Markku Sopanen for his help with theory of this work and reviewing the paper. I also thank Mona Mahboob Kanafi for providing samples for computer simulations.

Otaniemi, 3.8.2016

Alexander Permogorov

Contents

Symbols and abbreviations

Symbols

$\vec{E}$	electric field vector
$\vec{H}$	magnetic field vector
$\vec{k}$	wave vector
$\hat{k}$	unit length wave vector
$\tilde{n}$	complex refractive index
n_r	real part of complex refractive index
R	reflectance
T	transmittance
α	absorption coefficient
κ	extinction coefficient
ω	circular frequency
ρ	reflectivity
τ	transmissivity

Abbreviations

ABS	Anti-Blocking System
ACC	Adaptive Cruise Control
ESP	Electronic Stability Program
CW	Continuous Wave
DAQ	Data Acquisition
EM	Electromagnetic
FIR	Finite Impulse Response
LD	Laser Diode
NIR	Near Infrared Radiation
PD	Photodiode
SNR	Signal-to-Noise Ratio
STD	Standart Deviation

1 Introduction

Nowadays, road accidents are still a great problem in vehicle traffic. Among all other reasons, friction between vehicle tires and the road surface is not the least important. The greatest problem with it is that unlike atmospheric, lighting and traffic factors, drivers cannot estimate friction with bare-eye observation. In reference [1] a study was performed. In this study drivers were proposed to estimate road friction coefficient which then was compared to actual friction measurement data. Road friction conditions there were divided into four types: good grip ($\mu > 0.45$), fairly good grip ($0.35 < \mu < 0.45$), fairly slippery ($0.25 < \mu < 0.35$) and slippery ($\mu < 0.25$). When drivers' survey was compared to the friction measurements, it turned out that less than 30% of people's evaluations matched the measured values, and more than 27 % differed from them by 2 or 3 mentioned categories.

Another related experiment was performed in reference [2] in a VTI driving simulator. Two road designs were introduced with the friction coefficient of 0.8 corresponding to summer conditions. For winter conditions the coefficients were 0.8, 0.4 and 0.25. Results showed that compared to the summer conditions, the average speed decreased by 11-12 km/h and 16-17 km/h for the two virtual test track designs. In the same winter road, despite the different friction, average change of the chosen speed was within 1 km/h.

This means, that drivers evaluate the safe speed mostly on visual information in different weather conditions. In order to make driving safer, a helping system should be proposed. This system should either show the driver the friction coefficient explicitly, or somehow share friction data with the built-in car safety systems.

There is a huge variety of such systems. Some of them are utility vehicles driving on public roads. An attachable trailer is presented in reference [3]. Others estimate tire-road friction directly or evaluate the road surface and then friction is looked up in a database. These types of sensors will be described in chapter 2.

A potential application of friction sensors is not only showing the driver the actual friction coefficient. These sensors could, as mentioned above, communicate with intelligent car active safety systems such as adaptive cruise control (ACC), electronic stability program (ESP), anti-blocking system (ABS), and different collision mitigation and automatic emergency braking systems, or even upload to a data cloud to show friction measurements on an interactive map.

It can be clearly seen, that sensor providing road friction information is highly needed for road safety. The goal of this work is to present a commercial prototype of such a sensor. This means, that we need to find a compromise between the sensor cost, effectivity and reliability. Cost reduction has a huge influence on the chosen optic and electronic components of our device.

In this work a prototype upgrade for non-contact road surface evaluation by means of near infrared (NIR) radiation scattering and absorption is described. This prototype is expected to be able to distinguish four asphalt road conditions: dry, wet, icy and snowy.

In section 2.4 we discuss the optical properties such as asphalt surface reflection and absorption of dry and covered asphalt.

Next, the experimental setup and process are discussed. We present upgrades made to the prototype's optic and optoelectronic parts, show its electric circuit and discuss manipulations with the circuit. We also perform an experimental study of the prototype. This study includes measurement of back-reflected light intensity and its analysis in order to find consistent patterns, helping to determine road surface coverage. This topic will be elaborated in Section 3.3.

Further we compare the actual prototype measurement results with computer simulations for dry and wet surfaces. If results support each other, it will be possible to prove that the chosen methodology works and there is a possibility of further development of the prototype for the market.

To conclude our research, we discuss the ability of our sensor to determine road surface coverage and possible further upgrades to improve its accuracy.

2 Background

2.1 Means of Direct Tire-Road Friction Estimation

Some methods employ direct estimation of tyre-road friction coefficient, its maximum value in particular. These methods use the tire itself to perform measurements. The friction coefficient μ is introduced as the maximum value of ratio between the horisontal force F_H and the normal force F_N acting on tire-road contact area as

$$\mu = \frac{F_H}{F_N} = \frac{\sqrt{F_x^2 + F_y^2}}{F_N},$$

where F_x is the lateral force and F_y is the longitudal force. It is also possible to introduce slip angle (also called slip ratio) defined as the relative difference of a driven wheel's circumferential velocity $\omega_w r_w$ and its absolute velocity v_w

$$s = \frac{\omega_w r_w - v_w}{v_w}.$$

Slip occurs on driven wheels mostly while accelerating or braking due to wheel deformations. Following this definition slip ratio, zero slip corresponds to a free-rolling wheel, and the slip value of 1 to a locked wheel (as happens sometimes while emergency breaking).

Plotting friction coefficient vs. slip, actually, gives interesting results shown in figure 1.

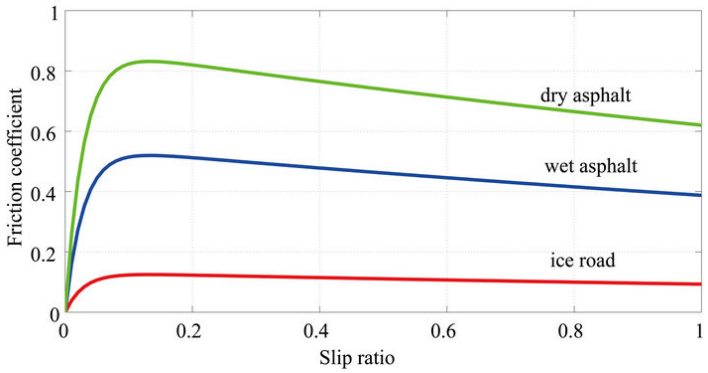

Figure 1: Plot of μ vs. slip ratio in different road conditions [4].

In this figure, we can observe, that function $\mu(s)$ shows a linear behaviour at small slip ratios and an explicit μ_{max} maximum value. This value is also called "friction potential". This is the maximum possible value of friction betweed tire and road surface. At normal driving conditions actual friction coefficient is smaller than potential friction. According to reference [5] it is possible to estimate μ_{max} through evaluation of slope of the linear part of $\mu(s)$.

It is quite impractical to directly measure the slip ratio and the lateral and the longitudal force direcly on a real vehicle. To overcome this complexity, the

measurement of tire deflection can eventually provide an estimate for both the slip ratio and the horizontal forces [6]. Many studies take advantage of this approach as it allows estimation of μ_{max}.

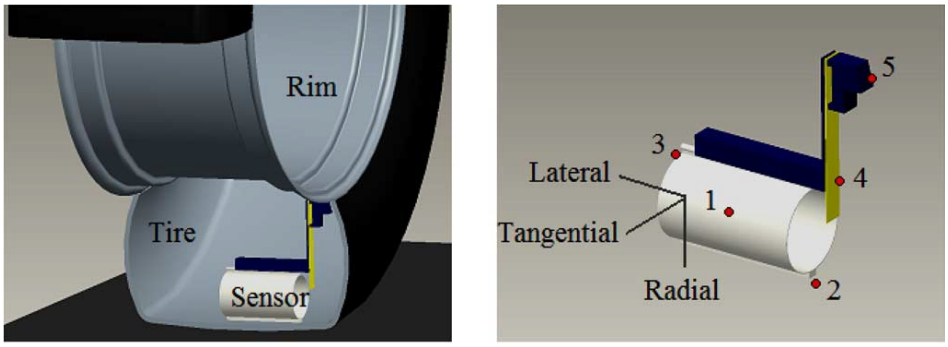

Figure 2: (a) Sensor location. (b) Designed tire sensor. 1: elastic component; 2: sensor base; 3: slider mechanism; 4: elastic cantilever beam; 5: root of cantilever beam [6].

For example, in reference [6] a piezoelectric sensor was inserted into the tire to measure exclusively the lateral deflection of the tire. If the value of lateral deflection is known, it is possible to use it to solve differential equations to calculate slip angle. Then the lateral force is estimated from the deflections. Considering the known normal force acting on the tire, it is then easy to compute μ and find $\mu(s)$ function for small slip angles. As mentioned in discussion above, it is then possible to estimate μ_{max}.Figure 2 shows the sensor position and the structure of the sensor.

It is also possible to measure tire contact patch deformation by meaning of changing electric capacity between metal cords [7]. When tire is deflected, cord displacement causes change the in measured capacitance, providing information about the displacement value.

Yet another method is described in reference [8]. There a laser-detector pair was used to measure tire carcass deformations. Both light emitter and the CCD matrix detector are mounted on the rim, and tread deformation causes deflection of laser beam registered by CCD. This resembles the principle of cantilever deflection used in atomic force microscopy. Figure 3 shows the schematic overview of this sensor. In that work aquaplaning conditions were compared to dry asphalt driving conditions. It was proved that by analyzing deflections, it is possible to detect aquaplaning with great confidence.

Unfortunately, the methodology of potential friction estimation through estimation of $\mu(s)$ slope in the linear region, and measuring tire deflection in particular, is not a robust approach, and it hasn't found its way into commercial market since its introduction in 1992 [9]. Generally, for different tires the $\mu(s)$ function is different for the same road condition. As a result, each method result, relying on tire deformation, depends on unique properties of the tire itself (including tire temperature and aging) and, hence, any sensor of this type needs to be calibrated for any unencountered before tire. Moreover, methods described above need a significant value of vehicle

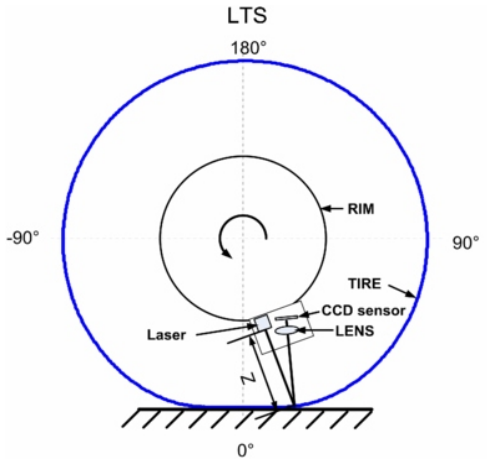

Figure 3: Schematic layout of a laser-CCD based tire deflection sensor [8].

acceleration to properly eastimate $\mu(s)$ slope in the linear region.

To overcome these complexities, it is possible to introduce tire-insentive methods. An approach was proposed in reference [10]. Surface-acoustic-wave (SAW) sensor was used to measure strain of the tread inside the tire-road contact patch. The sensor itself was attached to tire liner and was connected to tread element firmly with a pin. Again, tread deformations occuring during movement of tread element inside the contact patch allowed to estimate friction.

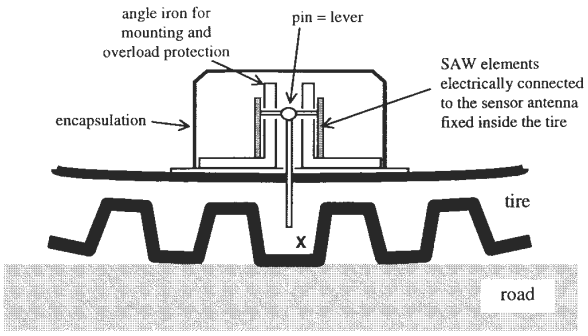

Figure 4: Experimental setup for tread element deformation measurement with SAW radio requestable sensors [10].

A way to estimate tire-road friction on a free-rolling tire was demonstrated in reference [11]. There three three-axis accelerometers were placed in such a way, that a solid piece of tire rubber was separating them from road surface. Location of the sensors and their axes are shown in figure 5.

A car with the tire, equipped with those sensors was tested on smooth surfaces with high friction (concrete) and low friction (ice). Data from the accelerometers allowed to form acceleration patterns for all three $x-$, $y-$ and $z-$axes. A bandpass filter was applied to obtained patterns, and then power spectrum was obtained in the range of 2000 Hz – 5000 Hz using discrete Fourier transform. It was shown that for ice-covered surface area under the power spectrum is significantly larger than for

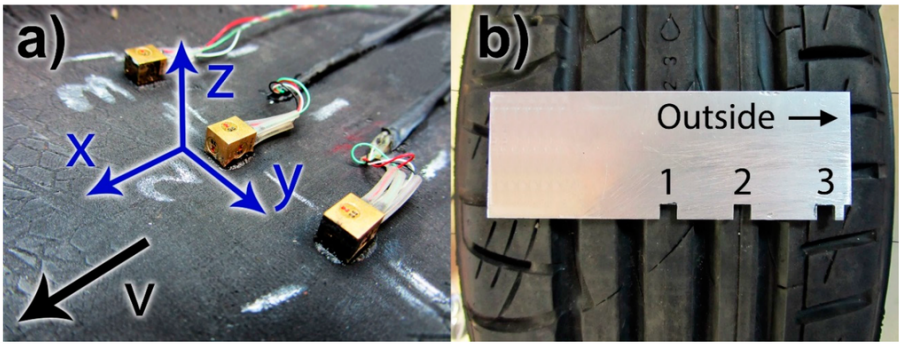

Figure 5: a) Accelerometers attached to the inner liner of the tire; b) Accelerometer positions in the tire (accelerometers attached to the inside) [11].

concrete surface. This method allows to detect low and high friction road conditions on a free-rolling tire, but there is a possibility that it also can be dependant on the used tire.

To leave tire properties behind, it is possible to measure forces on the tie rod of a car, like it was done in reference [12]. It was shown, that the relation between lateral force, acting on the tire in the contact pad, and aligning torque acting on it, does not depend on the lateral stiffness of tire rubber. This proves this method to be tire-insensitive. Piezoelectric force sensors mounted on tie rods of both left and right axels, providing information about aligning torque and lateral force acting on the tire.

Further estimations of friction potential require value of contact pad length. In this work contact pad length was measured with a pressure-sensitive film on a static tire. When contact pad length is known, it is possible to determine tire-road friction throug measurments, conducted by piezoelectric sensors.

2.2 Indirect Road Surface Characterization

It is common to analyze not the potential maximum value of friction coefficient, but analyze road surface itself or other indirect parameters, which are possible to measure during driving, and then provide some conclusions, depending on asphalt conditions.

A great example of such a different approach was shown in reference [13]. In this work, tire sound was recorded and processed to obtain high-frequency power spectrum. It was shown that under icy conditions, there is a measurable amplitude shift.

It is also possible to use EM radiation for analysis of the road surface condition. Such application of millimetre waves was shown in reference [14]. There depolarization of reflected light was measured to find ice coverage of the road surface.

In this work we are using NIR wavelength range radiation to determine road coverage. This method will be further explained in section 2.4. Now, there are a few commercially available products using this kind of radiation to estimate friction. The first of them is called "RoadEye" and is presented and described thoroughly in

reference [15].

Another model, engineered in a similar way comes from a company named "Teconer" [16]. This a device manufactured in Finland. It was not possible to find its operating mechnisms, but it is safe to assume that they are the same as in our prototype and the "RoadEye". Additionally, this sensor is claimed to measure contamination layer thickness.

A different axample of a similar device is manufactured by Lufft [17]. This sensor is claimed to not only determine variations in road conditions, but also measure road temperature, dew point temperature, relative humidity close to road surface, and covering layers' thickness within 0 – 6 mm range with 0.1 μm accuracy.

There is another way of engineering such a sensor. It is possible, for example, to use a NIR-sensitive camera instead of a single point detector. A sensor, using an InGaAs CCD matrix is presented in reference [18]. In that work the key was overlaying obtained NIR image with a regular (visible range) camera to determine road conditions not in a single point, but on in a square area with a size of 10×10 meters. Clearly, this sensor is a static one, and it should be mounted on a high post to cover such a large area.

In the beginning of the work, we describe common ways of tire-road friction estimation and state the necessary theoretical basis. This basis includes ray propagation and light-matter interactions. In this chapter we introduce derivation of Snell's law and Fresnel equations, and explain origins of light absorption in a medium.

2.3 Electromagnetic Wave Reflection and Absorption

Theoretical description of the methodology used in this work relies on scattering, absorption and reflection of EM waves on the boundary of two media with different complex refractive indices. Being a macroscopically rough surface with a feature size much greater than wavelength, we can treat every ray as specularly reflected one.

In this work we neglect microscopic scattering effects and choose ray approximation of light, combined with time-harmonic wave approximation with flat wavefront for every single ray. Moreover, we neglect the spectral width of the used light source and assume strictly monochromatic. Such an assumption lifts the necessity of considering different refraction angles in the same ray and different absorption in the rays coming from a single light source.

The incident ray in the sense of time-harmonic approximation can be described as a following 2-component vector

$$\begin{bmatrix} \vec{E}_{\shortparallel} = \vec{E}^0_{\shortparallel} \exp[i(\vec{k}\vec{r} - \omega t)] \\ \vec{E}_{\perp} = \vec{E}^0_{\perp} \exp[i(\vec{k}\vec{r} - \omega t)] \end{bmatrix}, \tag{1}$$

where $E_{\shortparallel}$ and $E_{\perp}$ denote field components parallel and perpendicular to the plane of incidence respectively and are connected to the total electric field as $E = \sqrt{E^2_{\shortparallel} + E^2_{\perp}}$ according to Pythagor's theorem. $E_{\shortparallel}$ and $E_{\perp}$ field components are also noted as p- and s- polarisations respectively. Plane of incidence is formed by the wave vector $\vec{k}$ and the boundary normal.

We can write the same exact relation for magnetic field $\vec{H}$

$$\left[\begin{array}{l} \vec{H}_{\shortparallel} = \vec{H}^0_{\shortparallel} \exp[i(\vec{k}\vec{r} - \omega t)] \\ \vec{H}_{\perp} = \vec{H}^0_{\perp} \exp[i(\vec{k}\vec{r} - \omega t)] \end{array}\right], \tag{2}$$

followed by analogical relation $H = \sqrt{H_{\shortparallel}^2 + H_{\perp}^2}$. Since we assume our waves transverse, vectors $\vec{E}$ $\vec{H}$ and $\vec{k}$ form a right-handed triad and each of them is orthogonal to the others.

In equations 1 and 2 $\vec{k}$ denotes the wave vector, showing propagation the direction of a given ray and $|\vec{k}| = 2\pi\tilde{n}/\lambda$. We can now denote $\hat{k}$ as a unit vector of the same direction as previously introduced $\vec{k}$

$$\vec{k} = \frac{2\pi\tilde{n}}{\lambda}\hat{k} = \frac{\omega\tilde{n}}{c}\hat{k} = \left(\frac{n\omega}{c} + i\frac{\kappa\omega}{c}\right)\hat{k}. \tag{3}$$

Here $\tilde{n}$ is complex refractive index and $\tilde{n} = n + i\kappa$, where n is the real part of refractive index and κ is called extinction coefficient.

Then we can substitute the derived value of $\vec{k}$ in terms of $\hat{k}$ from 3 into 1 and 2. Defining absorption coefficient as $\alpha = 4\pi\kappa/\lambda = 2\omega\kappa/c$ we can obtain following equations for the $\vec{E}$ and $\vec{H}$ components

$$\left[\begin{array}{l} \vec{E}_{\shortparallel} = \vec{E}^0_{\shortparallel} \exp[-\frac{\alpha}{2}\hat{k}\vec{r}] \exp[-i\omega(\frac{n}{c}\hat{k}\vec{r} - t)] \\ \vec{E}_{\perp} = \vec{E}^0_{\perp} \exp[-\frac{\alpha}{2}\hat{k}\vec{r}] \exp[-i\omega(\frac{n}{c}\hat{k}\vec{r} - t)] \end{array}\right], \tag{4}$$

$$\left[\begin{array}{l} \vec{H}_{\shortparallel} = \vec{H}^0_{\shortparallel} \exp[-\frac{\alpha}{2}\hat{k}\vec{r}] \exp[-i\omega(\frac{n}{c}\hat{k}\vec{r} - t)] \\ \vec{H}_{\perp} = \vec{H}^0_{\perp} \exp[-\frac{\alpha}{2}\hat{k}\vec{r}] \exp[-i\omega(\frac{n}{c}\hat{k}\vec{r} - t)] \end{array}\right]. \tag{5}$$

In this set of equations, the term $\exp[-\frac{\alpha}{2}\hat{k}\vec{r}]$ shows light absorption and the term $-i\omega(\frac{n}{c}\hat{k}\vec{r} - t)$ shows the phase at some particular time t in a given point in space.

At the interface (i.e., at the medium boundary plane) the phase of the propagating EM wave must be preserved and, thus, must not depend on the arbitrary choice of the coordinate and time scale origin. Therefore, for any given ray, we can demand the incident (i), the reflected (r) and the transmitted (t) components have equal phases

$$-i\omega(\frac{n_i}{c}\hat{k}_i\vec{r} - t) = -i\omega(\frac{n_r}{c}\hat{k}_r\vec{r} - t) = -i\omega(\frac{n_t}{c}\hat{k}_t\vec{r} - t) \tag{6}$$

This relation then can be simplified by eliminating the $-i\omega$ terms and t since time is equal for all of the described components, and $\vec{r}$ since for a single chosen ray its boundary projection is a point. Simplifications result in

$$n_i\hat{k}_i = n_r\hat{k}_r = n_t\hat{k}_t. \tag{7}$$

We have stated $\hat{k}$ as a unit direction vector. Obviously, for an isotropic medium all three $\hat{k}_i$, $\hat{k}_r$ and $\hat{k}_t$ lie in the exact same incidence plane, so we can evaluate their direction as

$$\begin{aligned} \hat{k}_i &= \sin\theta_i, \\ k_r &= \sin\theta_r, \\ k_t &= \sin\theta_t. \end{aligned}$$

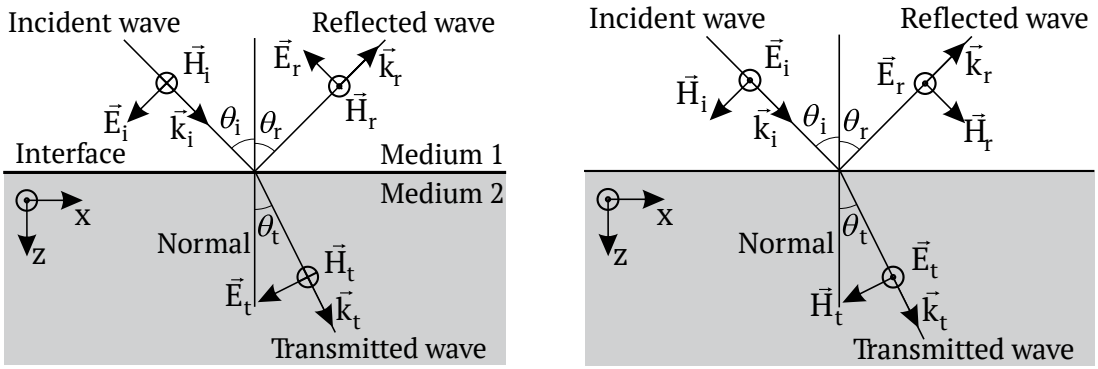

(a) $\vec{E}$ parallel to plane of incidence (p-polarization).

(b) $\vec{E}$ perpendicular to plane of incidence (s-polarization).

Figure 6: Illustration to s- and p-polarized incident rays [19].

Furthermore, we explore light propagation on the boundary of two media, so $n_i = n_r = n_1$ and $n_t = n_2$. We then can substitute these updated values of refractive indices into equation 7 and obtain the law of reflection and Snell's law:

$$n_1 \sin\theta_i = n_1 \sin\theta_r = n_2 \sin\theta_t \Rightarrow \begin{cases} \sin\theta_i = \sin\theta_r \\ n_1 \sin\theta_i = n_2 \sin\theta_t \end{cases}, \tag{8}$$

The Snell's law describes propagation direction of a light ray when it reaches an interface of two refractive media. There is a reflected part with an angle equal to the angle of incidence, and there is refracted part with an angle derived from refractive indices of the media and the angle of incidence.

For purposes of this work, it is essential not only to know ray directions, but also to extract light intensity after it has interacted with the interface. To achieve this, we can introduce parameters of reflectance ρ and transmittance τ for both parallel and perpendicular polarisation components as discussed in equations 1 and 2.

Maxwell's equations dictate that both the $\vec{E}$ and $\vec{H}$ components parallel to the boundary (tangential) must be continuous across the interface. To derive reflectance and transmittance we will calculate these values for two separate cases: $\vec{E}$ parallel to the plane of incidence (p-polarisation) or perpendicular to the plane of incidence (s-polarisation).

We will first treat the parallel case depicted in Figure 6a. Here, the boundary condition for the amplitudes of electric and magnetic field become

$$\begin{cases} E_i \cos\theta_i + E_r \cos\theta_i = E_t \cos\theta_t \\ H_i - H_r = H_t \end{cases} \tag{9}$$

If we incorporate $H = \sqrt{\frac{\epsilon}{\mu}} E$, coming from Maxwell equations for a flat time-harmonic wave, and an expression $n = c\sqrt{\epsilon\mu}$ for the refractive index into equation 9, we obtain

$$\begin{cases} E_i \cos\theta_i + E_r \cos\theta_i = E_t \cos\theta_t \\ n_1(E_i - E_r)/\mu_1 = n_2 E_t/\mu_2 \end{cases} \tag{10}$$

.

For most of the materials at optical frequencies $\mu_1 = \mu_2 = \mu_0$ and, thus, equations 10 can be simplified to a form of

$$\begin{cases} E_i \cos\theta_i + E_r \cos\theta_i = E_t \cos\theta_t \\ n_1(E_i - E_r) = n_2 E_t \end{cases} \tag{11}$$

Defining $\rho = \frac{E_r}{E_i}$ and $\tau = \frac{E_t}{E_i}$ and using equations 11 we obtain value for reflectance and transmittance at the media interface for case of p-polarisation

$$\rho_\perp = \frac{n_1 \cos\theta_t - n_2 \cos\theta_i}{n_1 \cos\theta_t + n_2 \cos\theta_i}, \tag{12}$$

$$\tau_\perp = \frac{2n_1 \cos\theta_i}{n_1 \cos\theta_t + n_2 \cos\theta_i}. \tag{13}$$

For the case of s-polarisation where $\vec{E}$ is perpendicular to the plane of incidence, we can show a set of equations analogical to equation 9.

$$\begin{cases} E_i + E_r = E_t \\ -H_i \cos\theta_i + H_r \cos\theta_i = -H_t \cos\theta_t \end{cases} \tag{14}$$

Ray propagation for this case is shown in figure 6b. From this set by repeating steps shown in equations 9 – 13 it is possible to obtain:

$$\rho_{\shortparallel} = \frac{n_1 \cos\theta_i - n_2 \cos\theta_t}{n_1 \cos\theta_i + n_2 \cos\theta_t}, \tag{15}$$

$$\tau_{\shortparallel} = \frac{2n_1 \cos\theta_i}{n_1 \cos\theta_i + n_2 \cos\theta_t}. \tag{16}$$

Applying the Snell's law to obtained reflectance and transmittance expressions in equations 12 – 13 and 15 – 16, we get a simplified version of these coefficients

$$\rho_\perp = -\frac{\sin(\theta_i - \theta_t)}{\sin(\theta_i + \theta_t)}, \tag{17}$$

$$\tau_\perp = \frac{2\sin\theta_t \cos\theta_i}{\sin(\theta_i + \theta_t)}, \tag{18}$$

$$\rho_{\shortparallel} = -\frac{\tan(\theta_i - \theta_t)}{\tan(\theta_i + \theta_t)}, \tag{19}$$

$$\tau_{\shortparallel} = \frac{2\sin\theta_t \cos\theta_i}{\sin(\theta_i + \theta_t)\cos(\theta_i - \theta_t)}. \tag{20}$$

In this study, though, we measure light intensity and not its amplitude. This leads us to the introduction of intensity reflectivity R and transmissivity T. It is known that $I \propto |E|^2$. Therefore, we can introduce $R = \frac{|E_r|^2}{|E_i|^2} = |r|^2$ resulting in

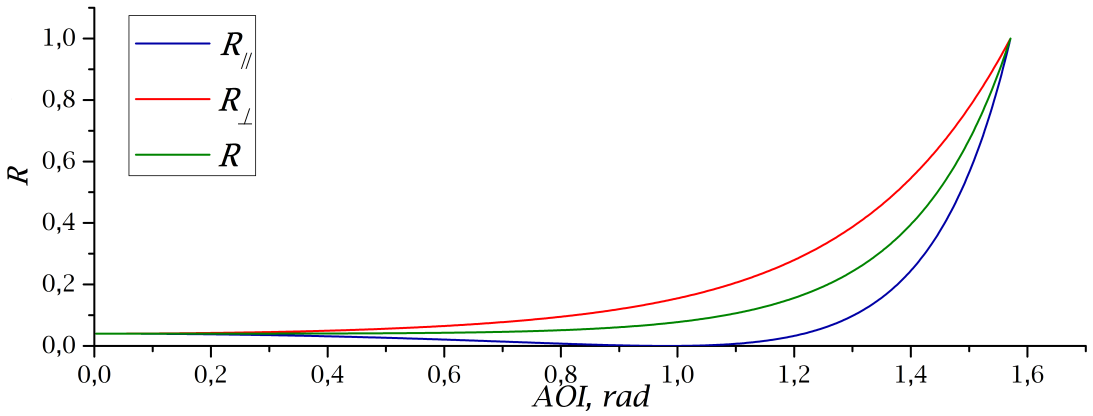

Figure 7: Plotted values for $R_{\shortparallel}$, $R_{\perp}$ and R from equations 21, 22 and 25, respectively.

$$R_{\shortparallel} = \frac{\tan^2(\theta_i - \theta_t)}{\tan^2(\theta_i + \theta_t)}, \tag{21}$$

$$R_{\perp} = \frac{\sin^2(\theta_i - \theta_t)}{\sin^2(\theta_i + \theta_t)}. \tag{22}$$

Afterwards, we can introduce intensity transmissivities as

$$T_{\shortparallel} = 1 - R_{\shortparallel} = \frac{4\sin\theta_i \sin\theta_t \cos\theta_i \cos\theta_t}{\sin^2(\theta_i + \theta_t)\cos^2(\theta_i - \theta_t)}, \tag{23}$$

$$T_{\perp} = 1 - R_{\perp} = \frac{4\sin\theta_i \sin\theta_t \cos\theta_i \cos\theta_t}{\sin^2(\theta_i + \theta_t)}. \tag{24}$$

In the case of our experiment we used unpolarised light, which means both s- and p-polarisation intensities are equal and total reflectivity can be shown to be

$$R = \frac{1}{2}(R_{\perp} + R_{\shortparallel}) \tag{25}$$

In figure 7 values of $R_{\shortparallel}$, $R_{\perp}$ and R are plotted vs. angle of incidence in radians. We can see in the figure that $R_{\perp}$ and R increase from 0 to 1 with the increase of angle of incidence. Howerver, $R_{\shortparallel}$ shows quite different behaviour. At a certain angle, light polarized in the plane of incidence is not reflected. This angle is called Brewster's angle and can be calculated as

$$\theta_{Br} = \arctan\frac{n_2}{n_1} \tag{26}$$

Geometrically, Brewster's angle corresponds to a situation, when the angle between incident and refracted (transmitted) rays is 90 degrees.

When light travels through a medium, it loses intensity through absorption. As already mentioned in equation 3, complex refractive index can be introduced as $\tilde{n} = n + i\kappa$, where n is the real part of refractive index and κ is the extinction

coefficient. When substituting such a value into the expression for electric field, we get

$$\vec{E} = \vec{E}_0 \exp[-\frac{\alpha}{2}\hat{k}\vec{r}] \exp[-i\omega(\frac{n}{c}\hat{k}\vec{r} - t)]. \tag{27}$$

Here the term $\exp[-\frac{\alpha}{2}\hat{k}\vec{r}]$ is a real exponent showing field decay during propagation through the medium and $\alpha = 4\pi\kappa/\lambda = 2\omega\kappa/c$ is the absorption coefficient. We can simplify equation 27 term by assuming straight propagation of light along z-direction and remembering that $\hat{k}$ was chosen to be a unit vector. These assumptions make the dot product $\hat{k}\vec{r} = z$. Then the expression for the electric field will take the form of

$$E = E_0 \exp[-\frac{\alpha}{2}z] \exp[-i\omega(\frac{n}{c}z - t)] \tag{28}$$

Then we can calculate the ratio of the transmitted and incident amplitudes. To do so, we simply divide them

$$\frac{E_t}{E_i} = \frac{E_0 \exp[-\frac{\alpha}{2}z] \exp[-i\omega(\frac{n}{c}z - t)]}{E_0 \exp[-\frac{\alpha}{2}z_0] \exp[-i\omega(\frac{n}{c}z_0 - t)].} \tag{29}$$

As we are generally interested only in the envelope amplitude, we can neglect time-harmonic parts of equation 29 and get for the amplitude

$$E_t = E_i \exp[-\frac{\alpha}{2}(z - z_0)]. \tag{30}$$

Since $I \propto |E|^2$, for intensity we get

$$I_t = I_i \exp[-\alpha(z - z_0)] = I_i \exp[-\alpha(\Delta z)]. \tag{31}$$

The unit of α is the inverted value of distance, and physical meaning of α intensity loss by e times.

Qualitatively light absorption in a medium can be described using the plane wave approximation and the Lorentz oscillator model – a driven damped harmonic oscillator. A monochromatic light wave can induce dipoles in the medium, shifting the electron cloud from positive nucleus, and force their oscillations with its own frequency ω. Dipoles in the material have their own resonant frequency ω_0. Generally, there is a finite set of such resonant frequencies, but, for the sake of this explanation, we will only consider one of them. For chosen dipole, oscillations are determined by equation

$$\begin{cases} m\ddot{\vec{x}} = -e\vec{E} - i\omega_0^2\vec{x} - m\gamma\dot{\vec{x}} \\ \vec{E} = \vec{E}_0 \exp[-i\omega t] \end{cases} \tag{32}$$

Solving this equation will give expression for $\vec{x}$

$$\vec{x} = \frac{-e\vec{E}_0/m}{(\omega_0^2 - \omega^2) - i\gamma\omega} \exp[-i\omega t] \tag{33}$$

Looking closely at equation 33 we can observe few important things. First, when $\omega = \omega_0$ denominator is minimal, which corresponds to the maximal oscillation amplitude and thus leads to resonance. Additionally, $x(\omega)$ is entirely imaginary at the resonant frequency ω_0 so there is a $\pi/2$ phase difference between the dipole oscillations and the driving field, also called phase lag.

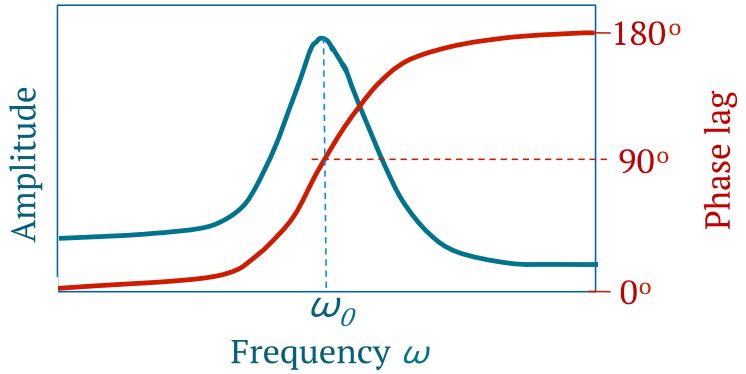

Figure 8: Plotted values for amplitude $|x(\omega)|$ and phase lag $\mathrm{Arg}(x(\omega))$ [20].

Secondly, at frequencies much higher than ω_0, the amplitude $x(\omega)$ is very small, and phase lag is π. At frequencies much lower than ω_0 $x(\omega)$ is finite and driven oscillations are in-phase with driving field. This can be seen easily if plotting $|x(\omega)|$ and argument of $x(\omega)$, as done in figure 8.

When a light beam propagates through a homogeneous medium, it interacts with multiple dipoles. Radiation from off-axis dipoles arrives late to the observation point P in figure 9. It is important to note, that for any observation point on the axis integration over all driven dipoles will result in an additional phase lag of $\pi/2$. Due to this additional phase lag, absorption happens when the phase difference between incident light (driving field) and dipole oscillations is equal to π.

Also, in a medium there is a possibility of light scattering from microscopic inhomogeneities. These can come from small foreign particles embedded in the medium or structural imperfections such as voids. Depending on the size of these imperfections, light can suffer Rayleigh or Mie scattering. Scattering may cause changing of direction and additional absorption of light. Unfortunately, it is impossible to predict locations of defects in water or in covered asphalt, so estimating volume scattering would be methodologically complex.

Nevertheless, as stated in reference [21], any isotropic surface gives statistically symmetric scattering of reflected light. This statement corresponds to our assumption of asphalt roughness features that are very dense, but significantly larger than the used wavelength. Then in this very model, since we are using ray approximation, it is enough to assume specular reflection from water and asphalt surface features with appropriate intensity loss for each ray.

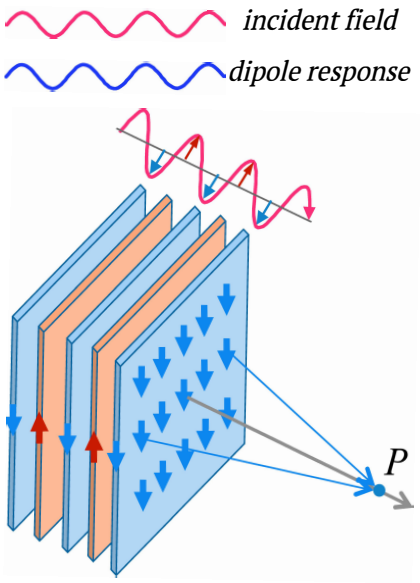

(a) Driven dipole oscillations in a bulk homogeneous medium.

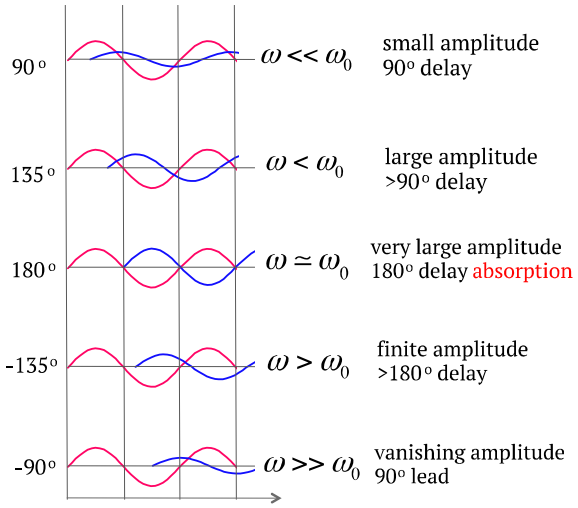

(b) Phase difference between the driving field and dipole oscillations.

Figure 9: Illustration of wave propagation in a homogeneous medium [20].

2.4 Near-Infrared Radiation Reflection and Absorption on Asphalt Surface

Building of the prototype as a part of this thesis is based on different scattering and absorption of dry asphalt and snow-, water-, and ice-covered road surfaces. Regarding scattering, two possible outcomes can occur during the experiment. First, there is diffuse scattering of light rays from the rough road surface. Second, if there is any transparent covering layer (i.e., water or ice), a significant fraction of light will be specularly reflected, and the remains will suffer absorption in the covering layer and diffuse scattering from the asphalt surface below. Additionally, some of the rays reflected from sample surface can experience full internal reflection and lose a great fraction of their intensity, which also decreases total reflected power.

In the experiment, three wavelengths were used – 1550, 1310 and 980 nm. For these wavelengths absorption coefficients of water and ice vary dramatically. Table 1 shows the values of α for these three wavelengths for water and ice.

Table 1: Different values of absorption coefficient α for liquid water [22] and ice [23]

Wavelength	Liquid Water	Ice
1550 nm	$12.100cm^{-1}$	$39.300cm^{-1}$
1310 nm	$1.530cm^{-1}$	$1.257cm^{-1}$
980 nm	$0.473cm^{-1}$	$0.143cm^{-1}$

The choice of wavelengths was determined by significant differences in refractive indices and absorption coefficients and the high commercial availability of laser diode sources with such central wavelengths. Refractive indices, which determine the

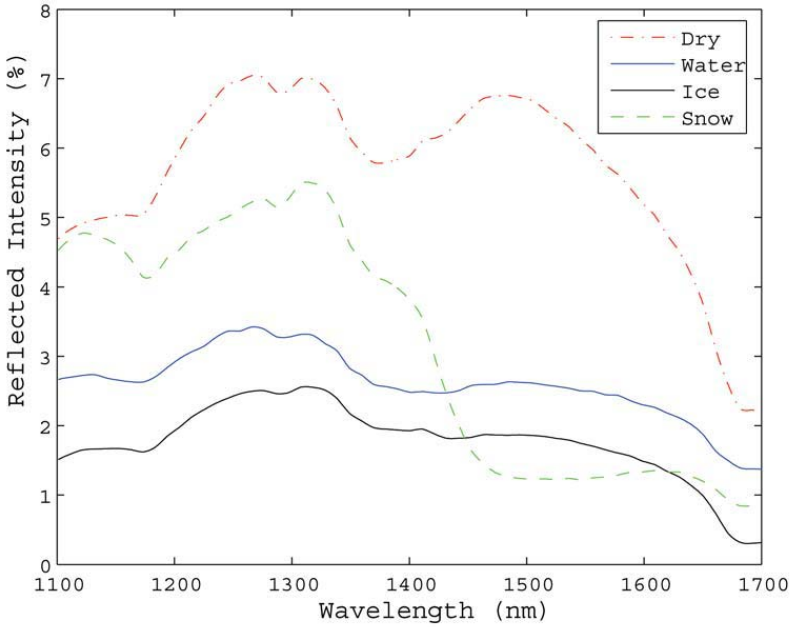

Figure 10: Spectral reflectance of covered asphalt for 1100 – 1700 nm range [15].

fraction of reflected intensity (see equations 21, 22, 25) are listed for used wavelengths in table 2.

Table 2: Different values of refractive index n and extinction coefficient κ for liquid water [22] and ice [23]

	Liquid Water	Ice
1550 nm	$n = 1.3154$ $\kappa = 0.00014925$	$n = 1.2906$ $\kappa = 0.00048474$
1310 nm	$n = 1.3200$ $\kappa = 0.00001595$	$n = 1.2958$ $\kappa = 0.00001310$
980 nm	$n = 1.3252$ $\kappa = 0.00000369$	$n = 1.3018$ $\kappa = 0.00000112$

Here we can see that for longer wavelengths α grows very much, especially for ice. Without a doubt, considering mechanisms mentioned above, icy surface would provide less backscattered power to the detector. Figure 10 shows the spectral reflectances of differently covered asphalt surfaces as functions of wavelength [15].

These spectra come from averaging reflectance measurements from a number of different angles between the light source and the detector. Also, thicknesses of covering ice and water were known, and then spectrum was averaged for different layer thicknesses. It is possible to see here that ice tends to reflect less than water, but the shape of the spectrum is almost tha same. However, in real-life applications, cover layer thickness is not known (see eqnuation 31), thus it is not possible to distinguish ice or water coverage through spectral reflectance measurements solely.

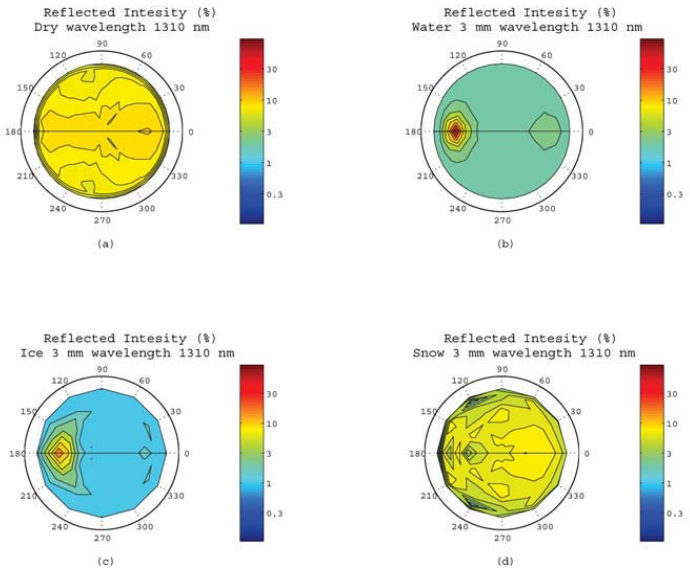

Figure 11: Scattering plot of dry, water-, ice- and snow-covered asphalt [15].

It is also quite noticeable for the snow covered surface that reflected intensity drops at approximately 1400 nm. This feature can be explained with nature of snow: it is formed with small ice crystals which according to Table 1 have strong absorption at longer wavelengths.

Detected backscattered power depends not only on absorption in the medium, but also on scattering from asphalt surface. For those four surfaces it is possible to introduce a scatter plot, shown in figure 11. It is seen that consistently to our model, dry asphalt shows diffuse reflection when the water- and ice-covered surfaces show dominating specular reflections. Snow-covered surface also shows diffuse reflections due to the snow layer composition.

The diffuse reflection profiles of dry asphalt and snow allow to approximate them as a Lambertian light source. This means that detected intensity will depend on the observing angle according to the Lambert's cosine law

$$I = I_0 \cos\theta$$

.

Snow is formed from small ice crystals with a size of approximately 0.1 mm according to reference [24] and are not densely packed. Thus we assume a finite air gap between any single flakes. Therefore, considering the illumination wavelength of 1 μm, particle size is approximately 100 times larger than wavelength, so ray approximation should stand. Light experiences multiple reflections and refractions at every snowflake-air interface. Since snowflakes are assumed to be oriented randomly with a uniform orientation distribution, each ray has an equal chance to be reflected in any direction. This model of a snow layer explains scatter plots shown in Figure 11 and further experimental results.

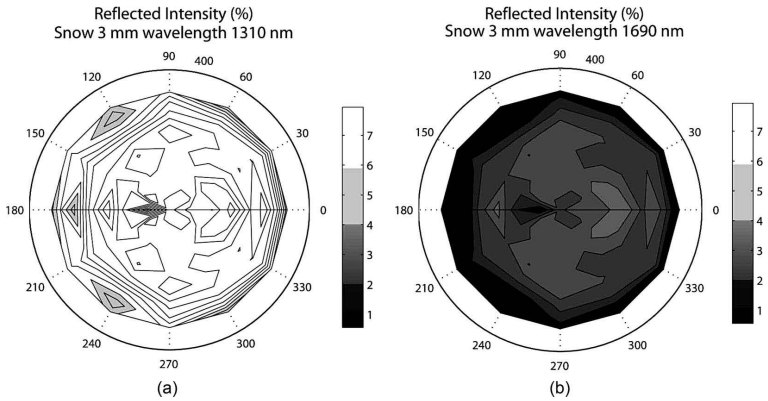

Figure 12: Scattering plot of illuminated snow-covered asphalt at the wavelengths of 1310 nm and 1690 nm [15].

Additionally, strong absorption of longer wavelengths by snow is depicted in figure 12. It is seen there that despite strong absorption, snow surface continues to show diffuse reflection.

Obviously, to compensate for asphalt roughness it is necessary for all of the three beams follow the exact same trajectories and have the same shape. Otherwise, each beam will reflect differently from the surface and thus different amount of power will reach detector. In the direction of this work, such a prototype configuration would be too complicated and expensive for commercial production. To overcome this problem, it is possible to average data gathered for each of light sources and get a mean reflected power value for a piece of the road surface. Such averaging is done under assumption that the asphalt roughness features are very dense and there is equal backscattered power for any straight paths of the same length chosen on the surface.

3 Experiment and Computer Simulations

One of the goals of this work was to improve an existing prototype model. To do so, several upgrades were made to its optical parts and electronical parts. In this section we will show the upgraded optical system of the sensor and the electronic circuit for continuous wave (CW) and modulated signal operation modes.

3.1 Optical and Electronical Components

3.1.1 Optical assembly

As a beginning, a condenser lens was introduced in front of the InGaAs photodetector. The lens focused incident light onto the sensitive area of the detector. This increased the effective detector area from 1 mm^2 to 62 mm^2. The lens also provide mechanical protection to fragile photodiode.

To improve the light source, collimators were introduced. Originally TO-can packaged uncollimated laser diodes show high beam divergence. In our case, this divergence had the value of approximately 20 degrees and the collimators reduced it to approximately 0.5 degrees. This collimated divergence angle corresponds to the beam spot diameter of 2 cm at the distance of 60 cm from the light source. The new prototype assembly is illustrated in figure 13.

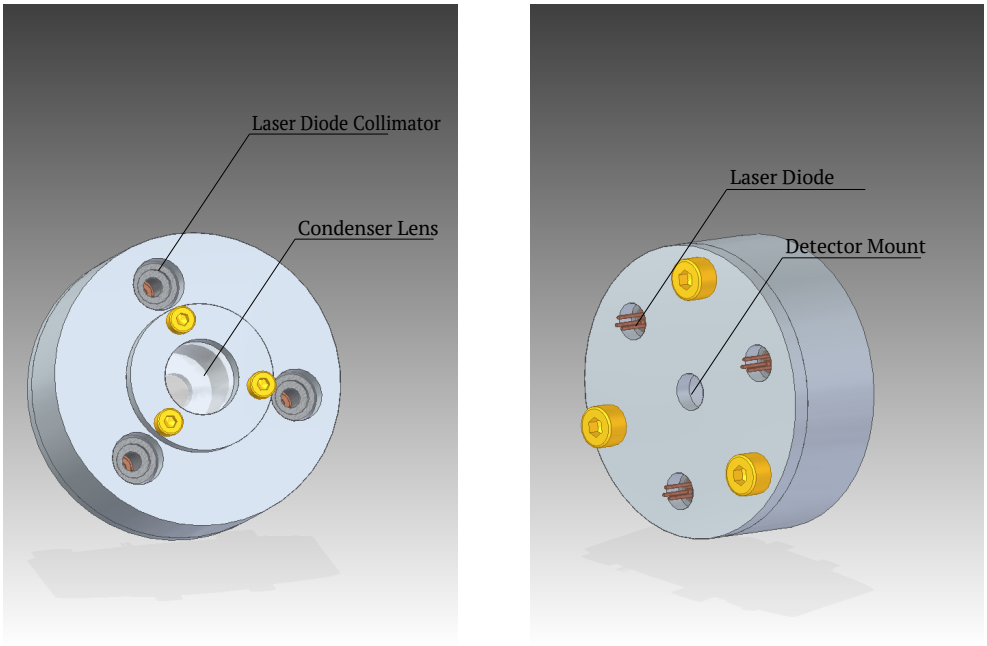

(a) Prototype assembly, front view. (b) Prototype assembly, back view.

Figure 13: Illustration of the prototype assembly.

For the light sources themselves, laser diodes (LD) were chosen. There are three LDs in the prototype, listed in table 3.

Table 3: Light sources used in prototype assembly.

Manufacturer	Part Number	Wavelength	Nominal power
Thorlabs®	ML925B45F	1550 nm	5 mW
Thorlabs®	ML725B8F	1310 nm	5 mW
Thorlabs®	L980P010	980 nm	10 mW

In order to hold the components of the renewed prototype, a new casing was machined. It holds the condenser lens and the photodiode at a distance equal to the focal distance of the lens. The optical axis of this system coincides with the rotation symmetry axis of the casing. The light emitters with added collimators are situated radially at distance of 12 mm from the axis. This made the whole system invariant relative to axial rotation of the sensor during installation.

3.1.2 Continuous Wave Mode Driving Circuit

Apart from optical components, the electric circuitry is also a very important aspect of the sensor. A new version of circuit was obtained directly through revising the circuit of the old version and correcting its flaws. As a result, the electronic component of the sensor can be divided in two main parts. The first part is laser driving circuit shown in figure 14.

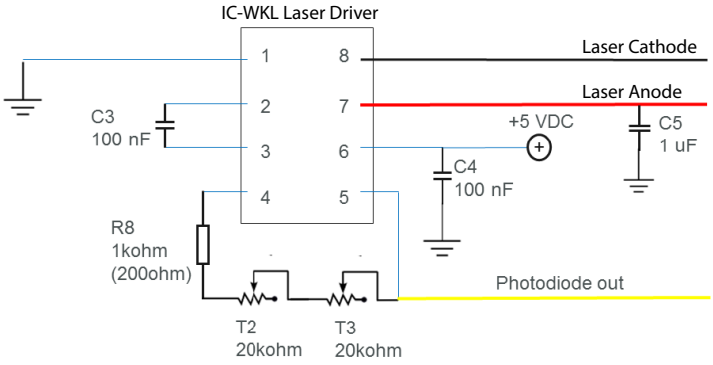

Figure 14: Electronic circuit diagram of the laser diode driver.

In figure 14 diode driver itself comes in a form of an integrated circuit (IC), which leaves only the surrounding elements to be placed manually on the prototyping board. In this figure, ports 7 and 8 refer to laser diode (LD) anode and cathode, respectively; ports 4 and 5 form a feedback loop. With potentiometers T2 and T3 it is possible to adjust driver output current in order to achieve the nominal power of the laser

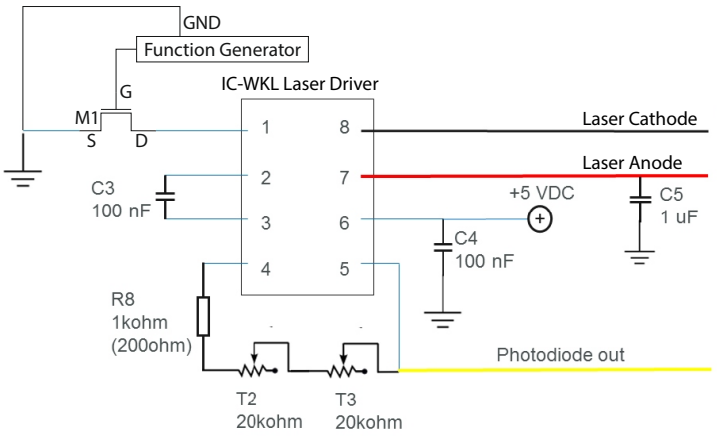

Figure 15: Laser Diode driver circuit drawing with modulation FET. M1 – transistor; D – drain; S – source; G – gate; GND – ground output of Function generator.

diodes. Capacitors C3, C4 and C5 have a role of stabilisation of output current since the LDs are very sensitive to large current fluctuations.

3.1.3 Modulated Signal Mode Driving Circuit

Originally, the circuit was meant to be operating in the continuous-wave (CW) mode. Such a mode of operation often gives lower signal-to-noise ratio (SNR) than using modulated signal. In addition, using a modulated light source in the prototype allows to use advanced signal processing techniques such as lock-in amplification. A lock-in amplifier can be introduced within the circuit or via software during final signal processing, like it was done in this work. Signal modulation was performed in a simple manner – an NMOS transistor was installed, replacing the ground wire of the laser driver. The modified circuit can be seen in figure 15.

The gate of the transistor M1 was connected to the signal output of a function generator (FG), and the FG ground was connected to the source of M1. This setup facilitated mudulation of the laser diode driver power supply with a signal from the FG. Since a MOSFET was used, the rectangular signal was produced by the FG. NMOS transistors have a threshold value of V_{GS} (gate-source voltage) opening the channel. Due to this, the usage of the sine wave complicates calculations of the duty cycle, while in the case of rectangular wave modulation it is seen explicitly. Schematic image of these modulations are shown in figure 16. During sine wave modulation, if the signal amplitude or the DC offset shifts, it may affect the duty cycle severely and thus compromize further processing. In this work rectangular wave was used. This waveform had the following characteristics:

- Frequency $f = 500\text{Hz}$,

- Duty cycle 50 %,
- DC offset = 0 V,
- Amplitude 5.5 V.

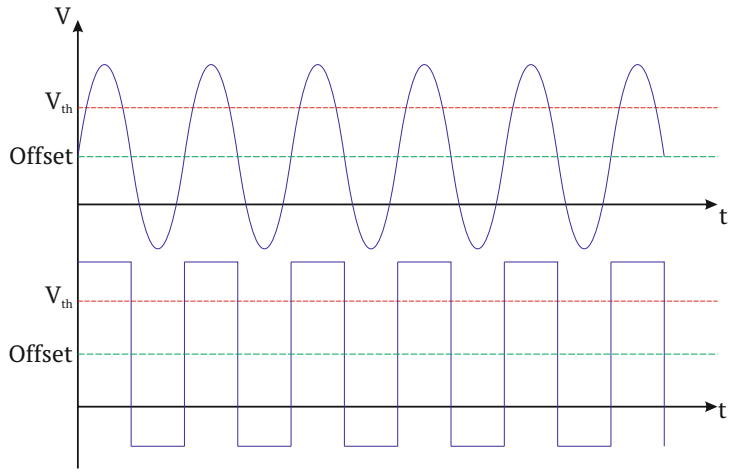

Figure 16: Shematic comparison of sine and rectangular wave modulation. V_{th} – threshold voltage; *Offset* – DC offset voltage.

3.1.4 Amplifier Circuit

Of course, an InGaAs photodetector gives a very small output current in order of few nA when small power is received. To make this current measurable, a preamplifier is introduced. Figure 17 shows the electronic circuit diagram of the preamplifier.

Here the photodiode PD is connected to an operational amplifier (OpAmp) as a current source. Supply voltage of ±15 V is coming from the OpAmp power supply, and the capacitors C1 and C2 are included to increase power stability. The gain of this preamp is determined by the negative feedback resistor R1 and has the value of 10^6. It is also necessary to have an amplifier circuit with adjustable voltage gain. Such adjustments allow calibration of the sensor to acquire adequate data. Figure 18 shows diagram of this circuit.

Here the potentiometer T1 regulates output voltage from the OpAmp. This adjustment can compensate for different levels of ambient lighting and provides a suitable ratio of signals gathered from the dry and covered surfaces, so that reflected intensities from both of the surfaces correspond to signal level higher than threshold, but lower than saturation.

Calibration of the sensor has two steps. At first it is necessary to adjust each laser (channel) power in order to have the same detector response in each of the channels. To do so, a white paper sheet was used. Typographic paper is a good Lambertian surface as it has purely diffuse light reflection. Each of the lasers was

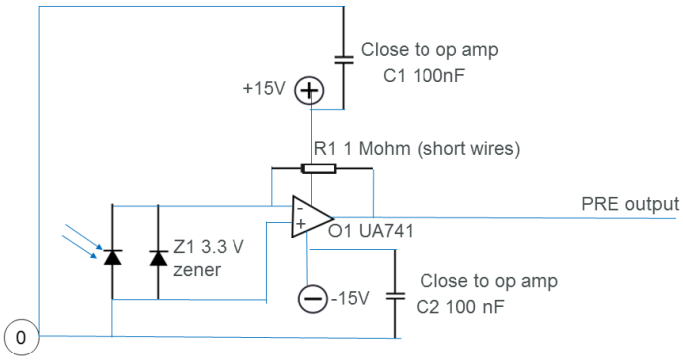

Figure 17: Photodiode preamplifier electronic circuit diagram.

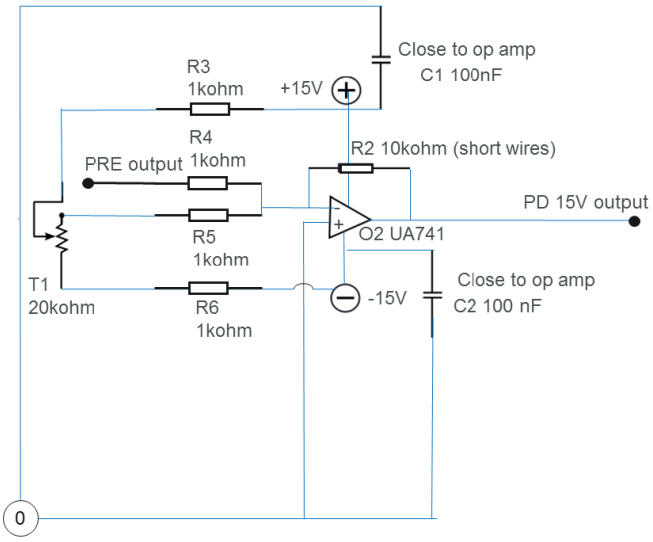

Figure 18: Photodiode postamplifier circuit.

then adjusted separately to provide the same amount of power backscattered to the photodiode regardless of their nominal power.

For proper experiment, it is necessary to assemble DAQ system. In this work National Instruments DAQ card model "NI USB-6210" was used and appropriate the LabView application was made. To ensure the highest possible amount of raw data for post-processing, the sample rate of the DAQ card was set to 100 kHz. For noise reduction purposes, every ten samples were averaged in LabView application, which reduced the sample rate to 10 kHz. This amount is enough for sensor movement at speed of approximately 1 m/s.

3.2 Experimental Setup Installation

In order to conduct measurements with the prototype, it is necessary to determine the optimal mounting angle and the height from the road surface. Fortunately, we had in posession a commercial sensor "RoadEye" described in [15], and it helped us to establish the optimal mounting parameters for the prototype.

The choice of the mounting angle is not difficult. A suitable step for convinient mounting angle is 15°, and the mounting angles are from 45° to the normal incidence angle (in future referred as 90°), leaving only four possible options. In order to determine the suitable angle, we can introduce a parameter "sum of mean intensities" (S). To compute it, data from each channel (a 1D array) gathered during a scan is merely averaged, and then such mean values for the three channels are added, resulting in the value of S, unique for all combinations of mounting angles and heights. The dependance of this parameter on the angle and the height is shown in figure 19.

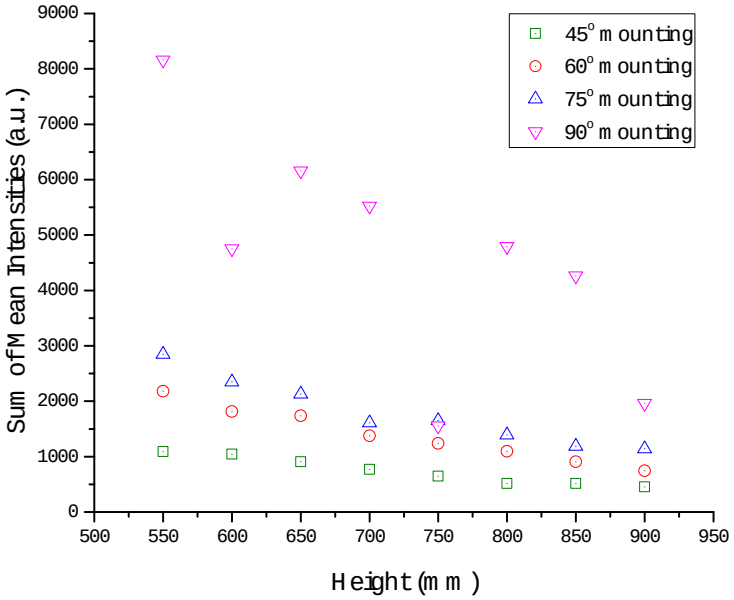

Figure 19: Sum of mean intensities registered by the detector at different heights of the sensor and different mounting angles.

Here it is easily seen that the angle of 90° gives a different behaviour of this parameter. SMI is higher, and there are outliers for heights of 600, 750 and 900 mm, if compared to the other cases. When at normal incidence, most of reflected light from a smooth surface reaches the detector, unlike at non-normal incidence angles. For specularly reflecting surfaces like water and ice, the detector gets overexposed at the angle of 90°. It is possible to overcome this problem by using an amplifier with adaptive gain as done in the R̈oadEye; but in this project we did not have enough time to properly implement it. If gain is adjusted manually, at normal incidence it is

impossible to get suitable signals for both the specular (ice and water) and the diffuse (dry asphalt and snow) cases without readjustments in the process of measurement, which is impractical. All of the prototype circuitry was designed in analog domain, and since such an adaptive amplifier is easier to implement in digital, this meant rebuilding all of the circuit.

All other mounting angles show similar behaviour if compared to each other. Reflected intensity slightly decreases with increasing mounting height. This happens due to non-perfect collimation of the light source beam. This beam has an initial divergence of approximately 0.5°, so with increasing distance less light reaches the detector. The asphalt surface is actually not a perfect diffuse reflector, but is very close to one, so for angles closer to the normal incidence the amount of reflected light is modestly larger according to the Lambert's cosine law. Having a measured map of heights of a real piece of the road surface, it is possible to check reflection behaviour of a sample with ray tracing. Reflected intensity in normalized units is shown in figure 20.

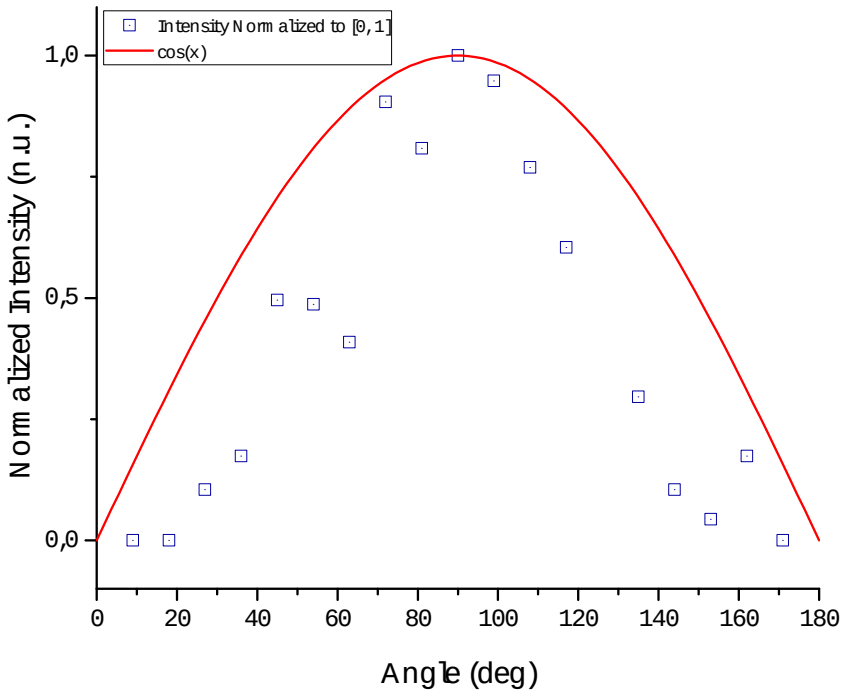

Figure 20: Dependance of normalized reflected intensity on observing angle.

In figure 20 we can see that reflection profile of a dry piece of asphalt resembles the reflection profile of a Lambertian surface. The red line in this figure shows function $y = \cos(x)$ within the interval of $0° - 180°$. We can also see here that the shape of the dependance of reflected light amount on observation angle is narrower than for an ideal diffuse reflector. This means that asphalt shows so-called mixed reflection. Some part of light is diffusely reflected, when remains are reflected specularly.

The mounting height was chosen to be 600 mm since this distance is the most suitable for most of the civil road-legal cars.

The object of investigation was a real piece of asphalt used on roads. This piece had rectangular shape with dimensions 25 cm × 100 cm. This sample was divided into four equal parts (25 cm × 25 cm) with ice-covered, snow-covered, water-covered and dry asphalt.

All the measurements were conducted in a cold chamber with temperature of −5℃ and relative humidity of 30 %. At this temperature and relative humidity it is possible to maintain water in forms of ice, snow and water simultaneously. Of course, such a low relative humidity caused faster evaporation of all the used covering layers than it happens in the street. However, speed of evaporation does not affect a single measurement since evaporation is much slower.

To create a water layer on asphalt in the cold chamber freezing conditions, salted water was used. An excess of salt was added so that the sodium chloride concentration in the solution was approximately 36 %. Such a concentration lowered the freezing point of water enough to keep it liquid in given conditions.

Ice was formed on the surface in a layer-by-layer manner with a sprayer. This method caused a formation of so-called "black ice" layer on asphalt. Black ice is a name for icy road when the ice layer is uniform, transparent, and does not include intrusions like air bubbles, cracks, etc. Basically, black ice is a flat uniform layer of ice on top of road surface compensating for macroscopic asphalt roughness. As a result the road surface becomes smooth.

Snow was collected in winter and preserved in a closed vial in a refrigerator. Fresh snow was collected before scheduled cleaning of public roads.

Mechanics of the measurement setup provided linear movement of the prototype along the asphalt sample. The sensor was mounted on a rail with the elevation of 60 cm from road surface. The laser beam produced by the prototype had an angle of incidence of 45° on the surface.

3.3 Signal Processing

3.3.1 Continuous Wave Signal Processing

As stated before, we decided to choose the installation height of 600 mm and the installation angle of 45°. In this chapter we will analyze the measurement results for different types of road surfaces obtained from measurements with a CW source and modulated source.

The first measurement analyzed is a CW mode one. The measurement included three scans for each of the wavelengths used. A representation of such a raw piece of data is shown in figure 21 below.

Figure 21 merely shows time evolution of signal obtained through the DAQ card. We can see there, that constant signal corresponds to sensor standing still. Sensor does not change its position because of delays between starts and ends of linear scans performed with the prototype and data acquisition. Changing signal corresponds to the scanning process. Even in this raw data representation it is possible to observe

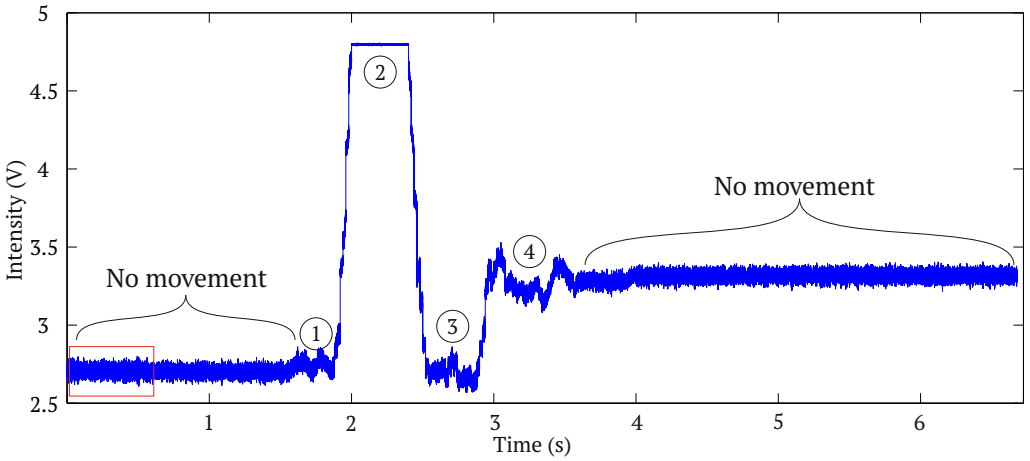

Figure 21: Raw signal time evolution collected from a single scan from 0.98 μm channel. Sample curface type division is shown as follows: 1 – icy surface; 2 – snowy surface; 3 – wet surface; 4 – dry surface.

different response of the sensor to different road conditions. We can see two sections with approximately the same signal level. These are ice- and water-covered parts of the studied sample. Dry asphalt response signal has moderate value. Response signal of the snowy surface shows the highest reflected intensity. It is seen in the figure that there is a significant amount of noise present. To remove it, it is possible to use one of the simplest digital filters – moving-average filter. Though it is possible to simply average unfiltered data received from the DAQ system, this requires the studied surface to remain constant during measurement. If the sensor operates in real-life conditions, this is not possible. A great benefit of using such a filter is that it can easily be implemented in hardware by using a digital signal processor (DSP). Moving average filter is a digital finite impulse response (FIR) filter, following equation [25]

$$y(i) = \frac{1}{M} \sum_{j=1}^{M-1} x[i+j] \tag{34}$$

where M is the size of the used averaging window (number of points in the average calculation), x is the input signal and y is the output signal. Equation 34 tells that n^{th} output value of the the filter is an arithmetic average of the w input values from n downwards. It is possible to notice that moving-average filter is actually a convolution of the input signal with a rectangular pulse having a unit area. Schematically, such filter is shown in figure 22. If following the flow of the block diagram, one can see that due to delay elements (noted as z^{-1} in the figure), as a result all of data points belonging to the window M of the filter are firstly divided by the window length, and then these resulting values are summed.

The gathered signal is time-domain, so, according to literature, the moving-average filter is an optimal choice, since it reduces random white noise and keeps a sharp step response. Noise reduction is equal to the square root of the window length. This kind of filter can also be used as a filter to eliminate white noise.

In figure 23 below the filtering result can be compared with the raw data. For

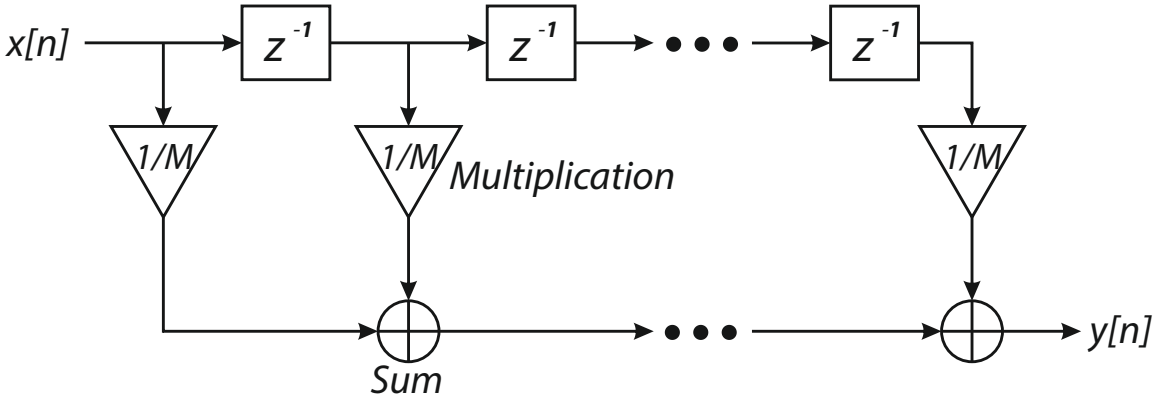

Figure 22: Block diagram of a moving-average filter. z^{-1} notation stands for a single step delay of an element.

convenience, the magnitudes are chosen to fit the area shown in figure 21 with red rectangle.

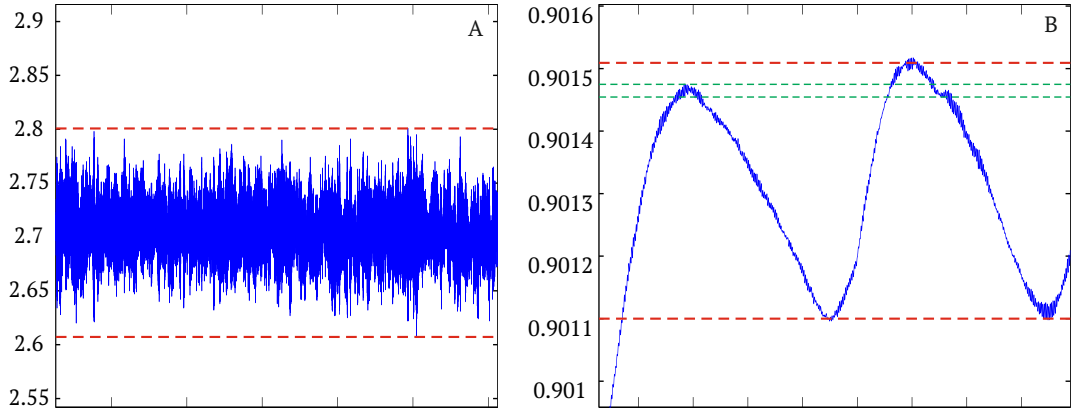

Figure 23: a) Magnified raw signal before filtering. The maximum noise amplitude in this range shown with the red line is 0.193; b) Magnified filtered signal. The amplitude of parasitic oscillations shown by the red lines is 0.0045.

In figure 23 after filtering parasitic oscillations occur. These oscillations are not related to the measurement features. However, the amplitude of these oscillations is negligible compared to the initial white noise amplitude. It is seen that filtering used not only reduces noise, but olso rescales the Y -axis of the measurement. It does not affect further calculations since they are all conducted in arbitrary units. It is though useful to compare noise before and after filtering. To do so, it is possible to introduce "normalized noise amplitude" parameter P_N. This parameter is calculated as the maximum noise amplitude on a section of a dataset over the mean value of this dataset or mathematically for a constant signal with random noise $S(t)$ in time interval Δt

$$P_N = \frac{\max_{\Delta t} S(t) - \min_{\Delta t} S(t)}{\overline{S(t)}} \tag{35}$$

For initial dataset this parameter $P_N = 0.0713$ and for filtered signal, predictably, $P_N = 0.0050$, more than ten times smaller.

Constant signal is used here for simplicity, and in the experiment it is easily obtained if the measurement is taken before the sensor movement starts. For example, such a signal is emphasized in figure 21 with a red rectangle.

After signal filtering for each channel, it is possible to plot the filtered raw data for all of three channels simultaneously. This requires the manual crop of each channel dataset but provides a great overview of the studied surface types.

3.3.2 Modulated Signal Processing

To reduce noise coming from the measurement, square-wave modulation was introduced. Due to circuit imperfections, some white noise with amplitude, proportional to the signal level, took place in the measured signal. These oscillations were successfully filtered by applying moving-average filter as described above. To filter white noise and preserve the shape of modulation filtering window was chosen to be small compared to the modulation period. The modulation period was 2 ms, corresponding to 200 data points after DAQ sampling of 100 kHz. Chosen filtering window of 5 data points proved the filter to be efficient in reduction of white noise and maintain the shape of the modulated signal. Figure 24 below shows comparison of initial and filtered signals. It is seen again that filtering rescales $Y-$ axis, but still it is obvious that filtering dramatically reduces parasitic oscillations.

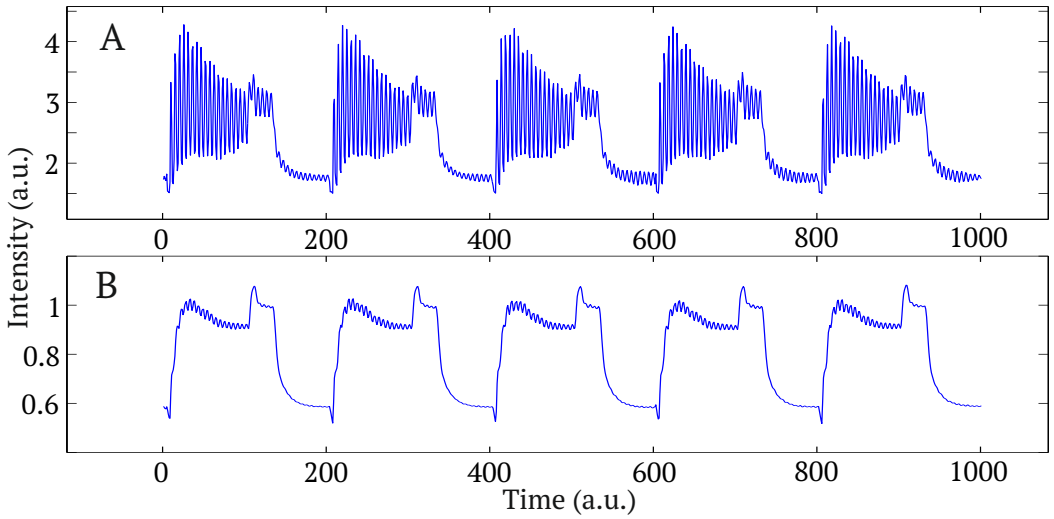

Figure 24: Comparison of a) Initial input signal and b) Initial signal after filtering.

To proceed further with signal processing it is necessary to demodulate the filtered input signal at the DAQ card. Demodulation allows to extract the actual data values. To do so, software digital lock-in amplifier was implemented.

Essentially, a lock-in amplifier is a piece of hardware or a software module acting as a filter with a large quality factor for a certain (reference) frequency. This provides

an opportunity to filter the signal efficiently and significantly improve SNR. In this work digital lock-in amplifier was implemented by using MatLab for signal processing.

The working principle of such an amplifier uses multiplication of modulated signal with the reference signal. Considering signal described by $V_{in} = V_s \sin(\omega_s t + \theta_s)$ and $V_{ref} = V_r \sin(\omega_r t + \theta_r)$ their multiplication will result in

$$V_L = \frac{1}{2} V_s V_r \cos([\omega_s - \omega_r]t + \theta_s - \theta_r) - \frac{1}{2} V_s V_r \cos([\omega_s + \omega_r]t + \theta_s + \theta_r) \tag{36}$$

In the case of equal frequencies of signal and reference waves $\omega_s = \omega_r = \omega$, equation 36 takes the form of

$$V_L = \frac{1}{2} V_s V_r \cos(\theta_s - \theta_r) - \frac{1}{2} V_s V_r \cos([2\omega]t + \theta_s + \theta_r) \tag{37}$$

The first term of equation 37 is now corresponding to the DC component with amplitude proportional to signal amplitude, and the second term to the high-frequency AC component which can be removed with a low-pass filter. If looking closer at the first term of $\cos(\theta_s - \theta_r)$ this equation, we can see that it is proportional to the phases of signal and reference. Obviously, the maximum output amplitude is obtained when the signal and the reference phases are synchronized. This can be done easily with phase shifter (hardware or software).

Schematically, lock-in amplifier configuration is shown in figure 25.

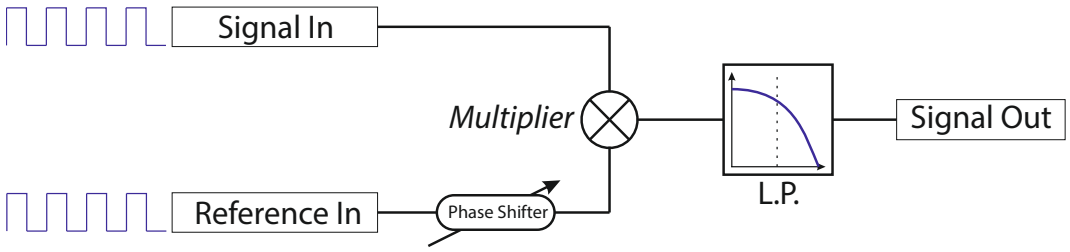

Figure 25: Block diagram of a lock-in amplifier. *L.P.* stands for low-pass filter. Phase shift is applied to reference signal.

In our work we used a square signal for modulation. A square signal can be represented by a Fourier series as an infinite sum of odd harmonics. Mathematically, it is presented as a function

$$[h] f(x) = \frac{4}{\pi} \sum_{n=1,3,5}^{\infty} \frac{1}{n} \sin(\frac{n\pi x}{L}) \tag{38}$$

Here L is the period of the square wave and n is the harmonic number.

In a digital lock-in amplifier multiplication of the square signal and reference waves gives a DC component that includes energy from all the present harmonics. Schematically, demodulation of the square waves is shown in figure 26 [26] below.

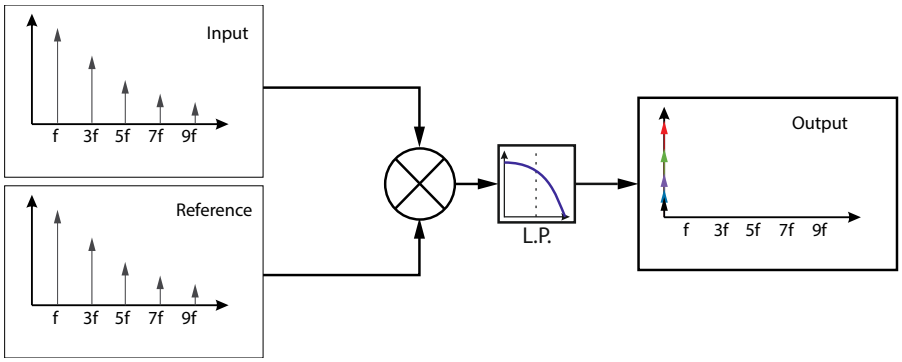

Figure 26: Frequency domain representation of square wave multiplication in a lock-in amplifier [26]; f is the frequency of the used square signal.

It is possible though, that if there is significant noise in one of the odd harmonics, it may affect the result of multiplication. However, in this work there was only a small amplitude of white noise present, so this issue was negligible.

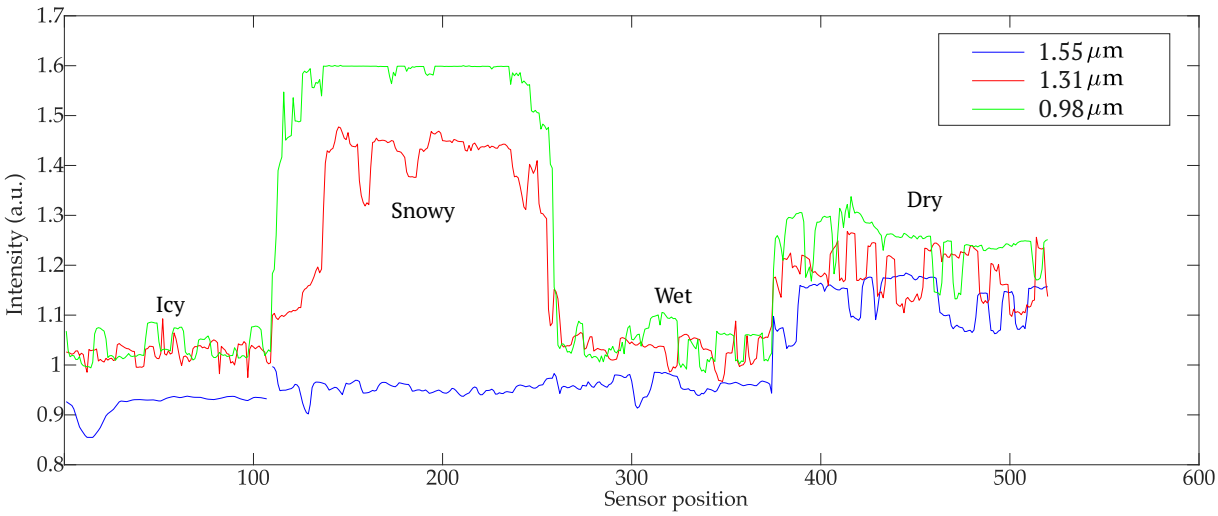

Figure 27: Pre-processed raw signal from measurements with modulation.

Here, the software lock-in amplifier was implemented in MatLab. The signal waveform was gathered from the DAQ as an array. This array is the measured data in time domain. The reference was constructed by the script as a square wave of the same period as the signal. The phase shift to match signal and reference phases was applied to signal waveform. This was done in the script by cutting first period of the signal. Of course, this action rersults in data loss, but, in our case, this loss is negligible.The low-pass filter following multiplication was implemented by taking the mean value of each period.

Analogically to the CW case, after filtering, demodulation and cropping of non-useful data (for example, points obtained when sensor is standing still) it is possible to compile pre-processed data from the used channels. This pre-processed data is shown in figure 27.

3.4 Computer Simulation Setup

The goal of the simulations is to compare quantitative results of the experiments with a representation of theoretical model. Hence, the simulation setup should be as close to conducted experiment as possible. To conduct simulations we used "Ray Optics" module of COMSOL Multiphysics. Such choice was determined by user-friendly interface of the software.

Computer simulations require large computational power. Since finite element modelling (FEM) is employed, there is a compromise present between the computation time and the model resolution. FEM approach means that the whole model used in simulations is converted into a mesh (in our case, free triangular mesh), and the computation times scale drastically with the element size and the number of rays.

To conduct simulations, a 2D model was introduced. This model uses a cross-section of the provided sample (a polygon converted to a curve object) and is bounded by an arbitrary experimental setup. This setup boundary is a requirement of the COMSOL version to provide a medium for propagation of light. Current approach does not facilitate propagation of EM radiation inside any area that does not have a closed boundary and specified optical properties. Apart from boundaries and the covering layer, the setup is filled with air. N_2 gas was chosen to represent it in the simulation since air contains 78 % of nitrogen. Simulation setup geometry fragment is shown below.

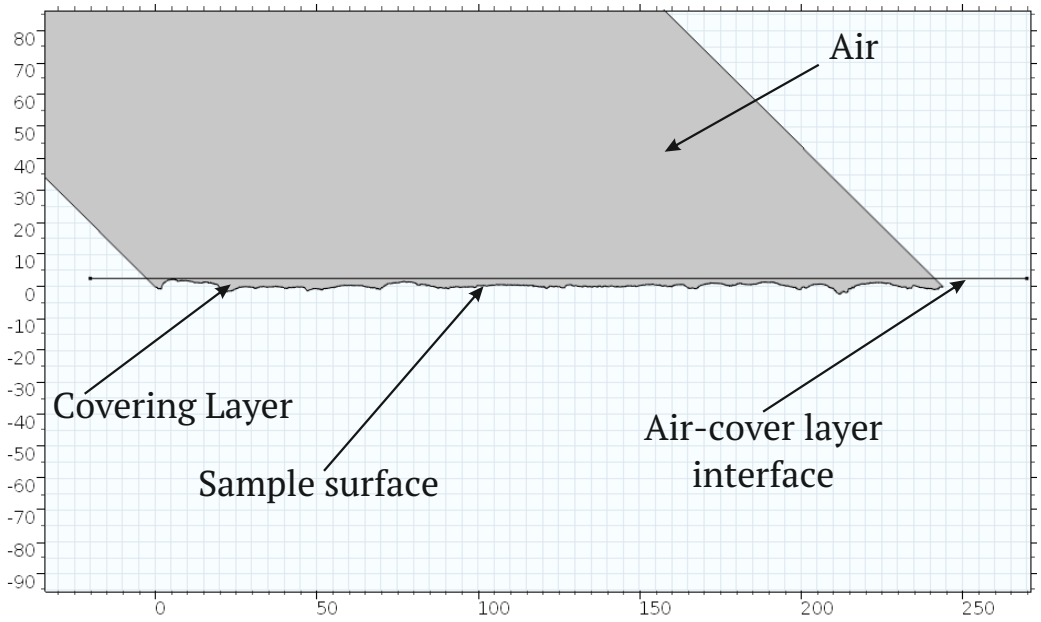

Figure 28: Schematic of the simulation setup, including a rough sample and the interfaces. Units of axes is mm.

Figure 28 omits the detector surface. Detector in the setup is merely a line segment.

The laser diode used in the experimental part showed a beam divergence of approximately 1° from the beam axis, which corresponds to a 20 mm diameter spot

at a distance of 600 mm from the source. To recreate this type of beam in COMSOL, we used conical beam with principal direction corresponding an angle of incidence of 45° and a divergence of 1°. This beam is split into rays. Empirically, 5×10^3 rays was found to be the optimal value. Each ray at any given point in time has a set of parameters describing it:

- A pair of spatial coordinates $[q_x, q_y]$ determining ray end position,
- A pair of wavevectors $[k_x, k_y]$ determining ray direction,
- Q_i determining ray power.

To calculate reflected intensities, source power was introduced. To get the simulation close to the experiment, light source power was chosen to be 5 mW. This value is equal for all the wavelengths used and close to original light sources' power used in the prototype. This power is divided equally between all rays released from the source.

Due to the relatively high ray density (linear distance between rays is 30 times smaller than surface features), purely specular reflection was chosen with 50% reflectivity for each ray at the surface. This assumption provides, from a macroscopic point of view, diffuse reflection shown by asphalt surface along with compensation for absorption. Strictly speaking, asphalt has its own spectral curve in the NIR spectral region [18]. In this work it is shown that for our wavelengths reflectivity does not experience significant changes, so choosing a constant value does not seriosly affect quality of simulation, but simplifies it well.

In the prototype, the detector was equipped with a condenser lens with aperture diameter of 10 mm. In the same manner, for simulations a detecting surface with length of 10 mm was introduced. Each ray reaching this surface was assumed detected and its power was added to the result. In COMSOL this was implemented by "Deposited Ray Power" attribute to the surface, following equation

$$Q = \frac{1}{A} \sum_i Q_i,$$

where Q is total ray power density, Q_i is single ray power, A is the area of the detecting surface. To get actual power from this expression, it is necessary to simply integrate resulting power density over detecting area.

It is important to recreate the experiment procedure in the simulation. In this particular case, we needed to perform linear movement of the sensor which included movement of both the light source and the detector. In the prototype, the light source and the detector do not coincide in space, but are close to each other compared to the distance of the sensor to the studied surface. For simlicity of the simulation setup, we chose ray release point to be situated in the center of the detecting segment. Both the light source and detector are moved simultaneously by using a parametric sweep. In this sweep, the parameter $q_{x,0}$ is responsible for linear movement, providing coordinates of the release point and the detector center. The chosen asphalt sample is 43 mm wide and 244 mm long, and its cross-section used in the simulation is taken

parallel to its long side. This said, $q_{x,0}$ is changed from $q_{x,0} = 5$ mm to $q_{x,0} = 239$ mm having 50 equally distributed points, where evaluation of the model takes place. The boundaries for the $q_{x,0}$ sweep differ from the sample boundaries by half-width of the detector segment. The parameter $q_{y,0}$ remains constant at 600 mm for the whole simulation. An illustration of this linear scan is depicted in figure 29.

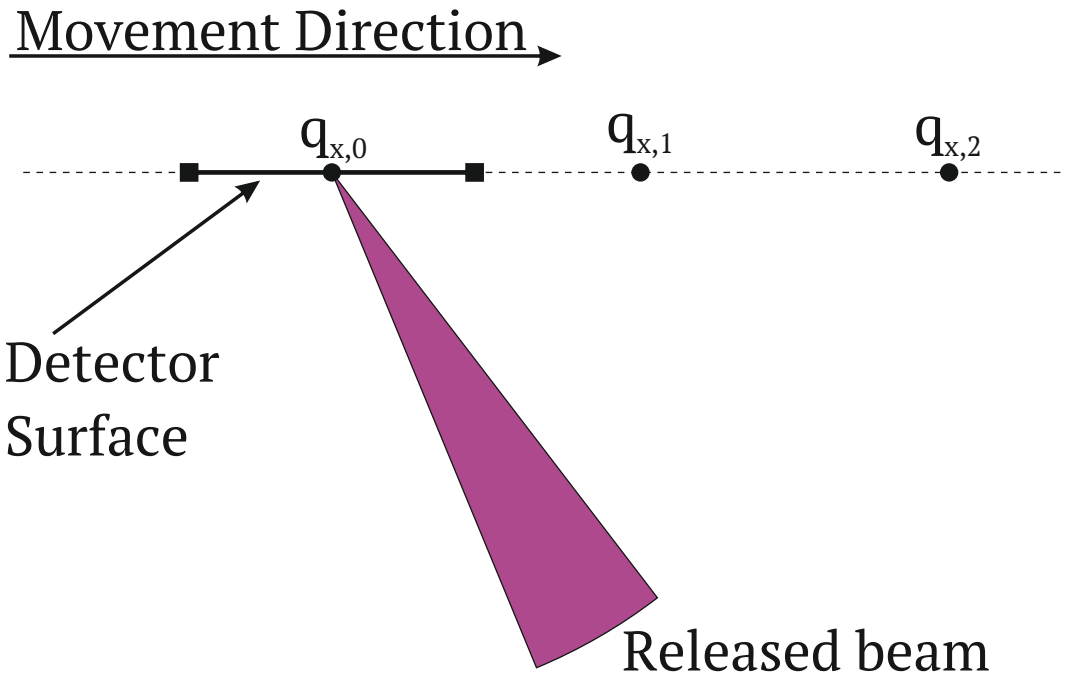

Figure 29: Schematic representation of the parametric sweep in simulations.

After release the rays propagate in the medium according to simulation assumptions predefined in COMSOL:

$$\frac{d\vec{q}}{dt} = \frac{\partial\omega}{\partial\vec{k}}, \tag{39}$$

$$\frac{d\vec{k}}{dt} = \frac{\partial\omega}{\partial\vec{q}}. \tag{40}$$

For homogeneous isotropic media used in our simulations, equations 39 and 40 mean straight propagation of light rays. When light reaches a wall of the simulation layout, there are few possibilities.

The first case is material discontinuity. This is the boundary between air and asphalt covering layer. Since these are two media with different refractive indexes, laws of reflection and refraction take place, and ray propagation is calculated accordingly. To calculate the ray powers Fresnel's equations (see equations 21 – 24) are used.

At the asphalt surface specular reflection was chosen. Such a reflection follows an equation

$$\begin{bmatrix} \vec{k}_{r,v} = \vec{k}_{i,v} \\ \vec{k}_{r,u} = \vec{k}_{i,u} - 2|\vec{k}_i|\cos(\theta_i) \end{bmatrix}. \tag{41}$$

In this equation an additional set of coordinates is introduced. u is the axis tangental to the surface at a point of incidence, v is normal to the surface. The angle of incidence θ_i is measured from the surface normal. As mentioned above, each ray loses 50 % of its power when reflected.

At all other walls apart from the detecting segment rays disappeared. This means that upon reaching a wall with this condition all information about this ray is deleted from the memory. Since these rays are of no interest to us in this modelling, it is good to clear computer memory to save useful resources.

Finally, the detector surface has "Freeze" boundary condition. This means that for rays that have reached this wall, their position, wavevector and power are stored. An attribute to this wall is called "Deposited Ray Power". This attribute allows future calculations of ray power reaching the detector.

4 Results and Discussion

Experiment and computer simulations provide data, showing the amount of backreflected light from dry and covered asphalt surfaces. In this section we will show ways of manipulating the data to determine road coverage, compare experimental results with computer simulations and discuss further improvements that can possibly be introduced in future.

4.1 Continuous Wave Mode Measurement Results

The initial raw data gathered by the sensor can be presented as shown in figure 30

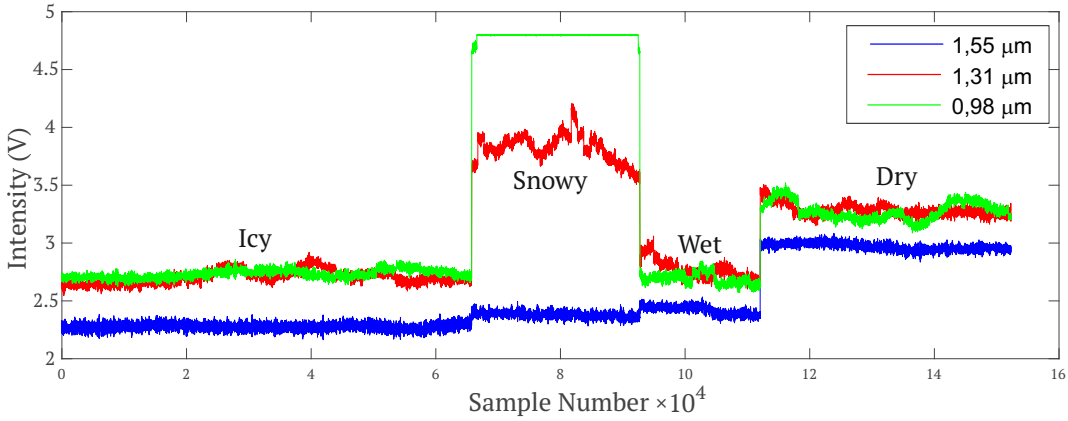

Figure 30: Raw unfiltered data as seen by the DAQ system for each of the channels.

In this figure detected intensity is actually voltage signal provided by the postamplifier. Even before filtering we can see predicted behaviour of different surface response. Surface response will be discussed shortly relying on the filtered data. In general, 1550 nm channel signal level is less than one of 980 nm and 1310 nm channels. The main reason is probably inferior collimation of 1550 nm radiation by conventional laser collimators. Poor, compared to 980 nm and 1310 nm wavelengths, collimation also leads to compensation of sample roughness. Large beam spot at the sample surface results in automatic averaging of illuminated surface roughness. One can notice significant amount of noise in each of the channels.

After signal filtering for each channel, shown in section 3.3.1, it is possible to plot the filtered raw data for all of three channels simultaneously. This dataset provides a great overview of the studied surface types.

In figure 31 we can see that for wet and icy surfaces reflected intensity is lower as predicted previously. Data for all of the surfaces except for snow show variations of reflected intensity due to large asphalt roughness features below the transparent covering layer. We can also see different shapes of reflected intensity during the linear scan of snowy surface. For 980 nm, there is overexposure of the detector. Despite prior calibration of the sensor on a piece of white typographic paper (see section 3.1.4), snowy surface returned a large enough fraction of light to cause saturation of the amplifier. For 1310 nm channel, absorption is seen compared to the 980

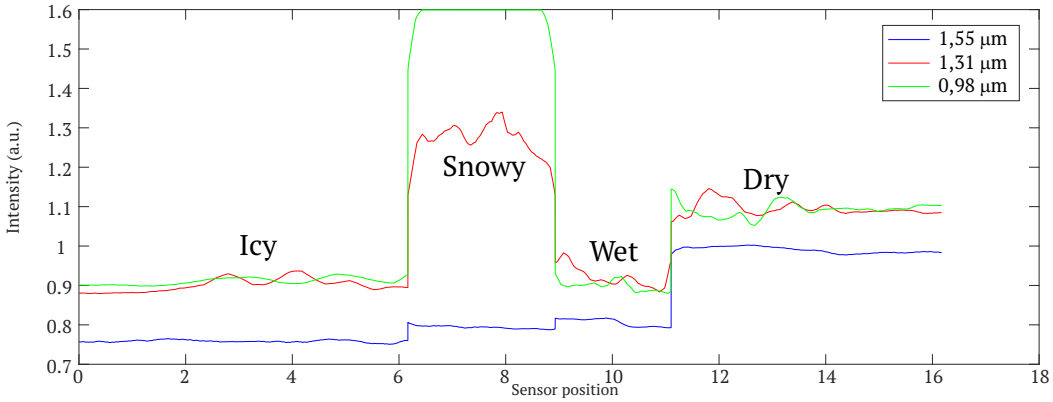

Figure 31: Raw filtered data for each of the channels.

nm channel. One can also notice that during the scan, amount of reflected light is proportional to the sample topography. This can either be a response to non-flatness of the snow surface, or response to asphalt roughness below the snow layer. Reflected intensity for 1550 nm channel is the least. In the case of the snow-covered surface, due to a lot of scattering, light travels a greater distance in snow compared to the uniformly-covered icy surface, so the difference in absorption for the three used wavelengths is seen clearly.

Finally, we can observe different shapes of surface-specific signals for the three channels. These different shapes occur due to different optical paths of each channel radiation. Additionally, it is possible to notice that different surface types are of different length. This happens due to difference of scanning speeds of each surface type piece. Such a speed difference comes from manual movement of the sensor.

To compensate for roughness-caused data variations, it is possible to plot mean values of the filtered signal for each of the surface types. This can be seen in figure 32.

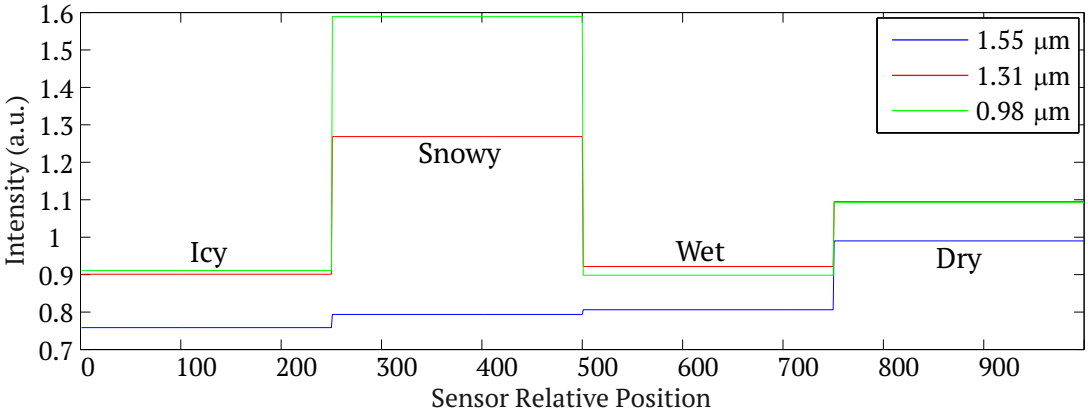

Figure 32: Mean values of filtered detected intensity for the studied surface types.

To properly show deviations from the mean values for each of the surface types, we can calculate standard deviations (STD) of the filtered signal for each surface and for each of the channels.

Table 4: Standard deviations for the studied surface types for each of the used channels.

	$1.55\mu m$	$1.31\mu m$	$0.98\mu m$
Dry	0.0077	0.0169	0.0167
Wet	0.0097	0.0257	0.0119
Snowy	0.0037	0.0420	0.0290
Icy	0.0031	0.0164	0.0089

In table 4 a smaller STD most probably results from inferior collimation of the 1.55μm channel compared to the other channels. A wider spot at the sample surface causes natural averaging of the asphalt roughess resulting in smaller STD values.

If looking closely at figure 31, we can notice that reflected intensity changes dramatically for specular- and diffuse-reflecting surfaces. This means that the very first step in distinguishing the road surface type is to compare these detected intensities. To do so, we introduce the parameter S – "sum of averaged intensities". Its value is merely a sum of the average reflected intensities of all the channels. For each of studied surface types, this parameter has a certain value. In figure 33 S is plotted for different surface types with single standard deviation. Using single STD value gives confidence boundaries of 95 %. We can see in this figure that S of dry and snowy asphalt is easily distinguishable from wet and icy surfaces. This means that S parameter calculation allows us to determine icy-wet and snowy-dry pairs. This is the first step of resolving the type of road surface coverage. To resolve surface types inside mentioned pairs, another method should be proposed.

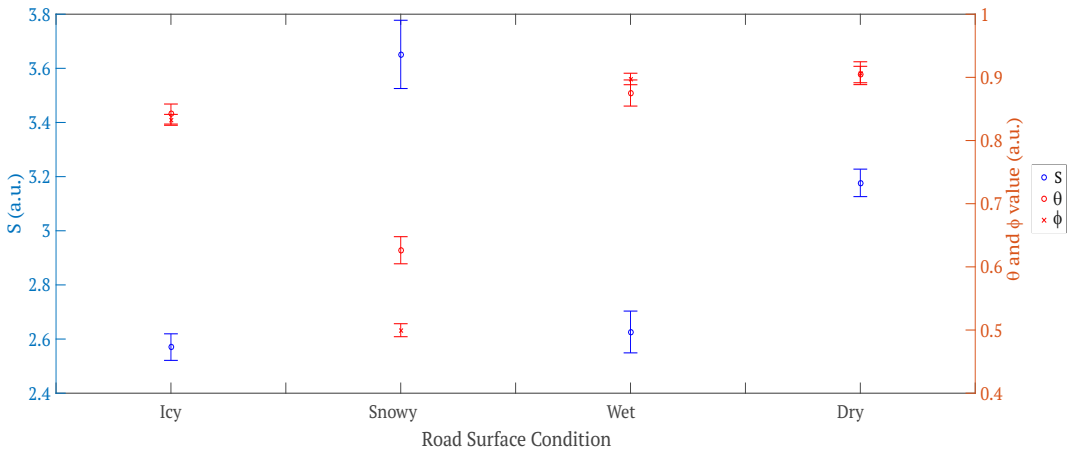

Figure 33: Errorbar plot of S parameter value for the studied surface types (left axis); Errorbar plot of θ and ϕ parameters for the studied surface types(right axis). Both plots represent values, corresponding to installation height of 600 mm.

Inspired by reference [15], two additional parameters were introduced. These parameters show ratios of channel intensities. Consider light source wavelengths of $\lambda_1 = 1.55\mu m$, $\lambda_2 = 1.31\mu m$ and $\lambda_3 = 0.98\mu m$. If I is the detected channel intensity,

then the ratios can be defined as

$$\theta = \frac{I_{\lambda_1}}{I_{\lambda_2}}$$

$$\phi = \frac{I_{\lambda_1}}{I_{\lambda_3}}.$$

Basically, these parameters directly show ratio between reflected intensities. Surface-divided mean values of these parameters with standard deviation are shown in figure 33 as an errorbar plot.

In figure 33 it is easily seen that the values of both θ and ϕ parameters stand out for the snowy surface. Such a ratio stands for all of the tested sensor installation heights. Therefore, this is the second criteria to resolve the snowy-dry pair successfully.

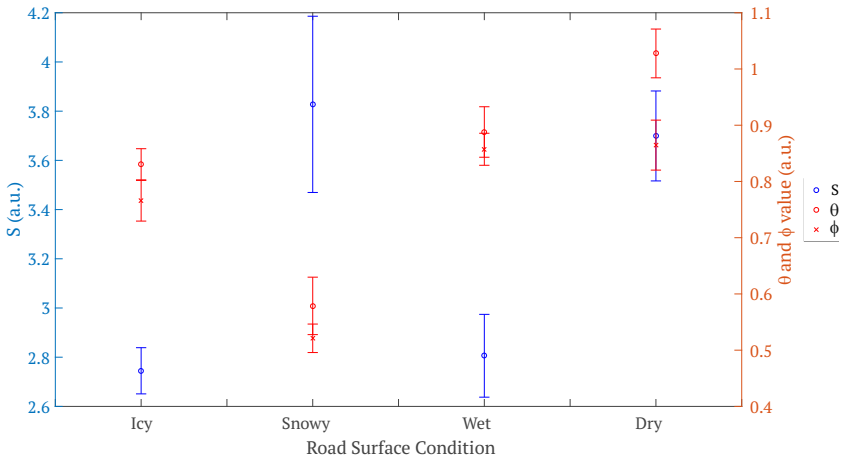

Figure 34: Errorbar plot of S parameter value for the studied surface types (left axis); Errorbar plot of θ and ϕ parameters for the studied surface types(right axis). Both plots represent values, corresponding to installation height of 400 mm.

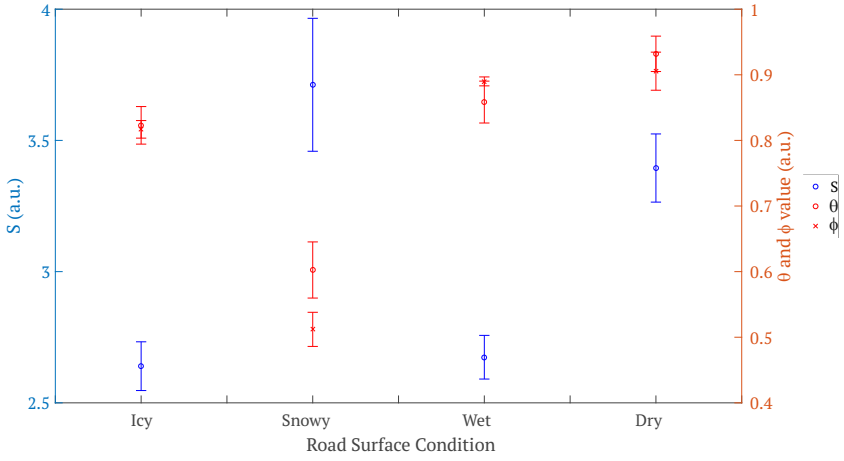

Figure 35: Errorbar plot of S parameter value for the studied surface types (left axis); Errorbar plot of θ and ϕ parameters for the studied surface types(right axis). Both plots represent values, corresponding to installation height of 500 mm.

It is necessary, though, to compare experimental results of different installation heights. During real life applications relative height of the sensor to the road surface may change due to vehicle height itself, or due to thickness of contamination layer on the road. Below, in figures 34 and 35 we can see data for sensor installation heights 400 mm and 500 mm.

We can see in figures 34 and 35 that for all of the introduced parameter, their relative distribution is the same for all of used installation heights. This means, that it is possible to use them to determine road surface condition and resolve dry, snowy and wet/icy conditions.

4.2 Modulated Signal Mode Measurement Results

Analogically to the CW case, after filtering, demodulation and cropping of non-useful data (for example, points obtained when sensor is standing still) it is possible to compile pre-processed data from the used channels. This pre-processed data is shown in figure 36.

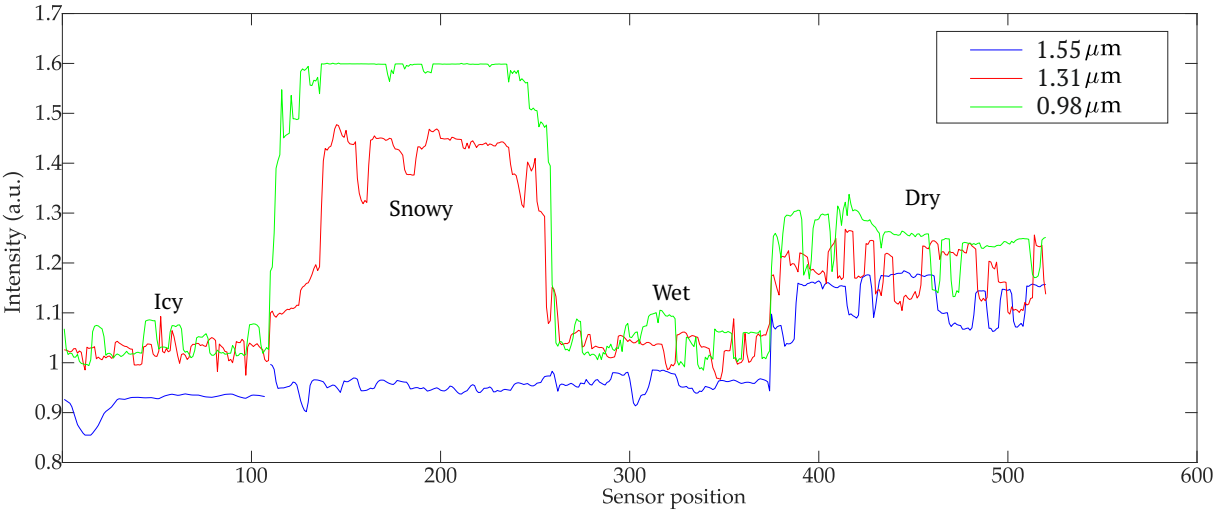

Figure 36: Pre-processed raw signal from measurements with modulation.

Data coming from the CW (see figure 31) and modulated signals (see figure 36) does not show qualitatively different behaviour in these two cases. This means that it is possible to use introduced S, θ and ϕ parameters in the same manner as previously.

First, we should look at S parameter. It is plotted in Figure 37 below.

Behaviour of the S parameter for modulated light measurement is the same as for the CW measurements shown in figures 33, 34 and 35. To justify the further use of S parameter, we can compare the modulated signal S parameter for the installation height used here (600 mm) to the other tested installation heights. Distribution of parameter values for those heights are shown in figures 39 and 40.

For the modulated signal we should also check parameters θ and ϕ. These are calculated in complete analogy with the CW signal processing. Using the definition of these parameters, we can plot the "raw" values of them. This plot will reflect

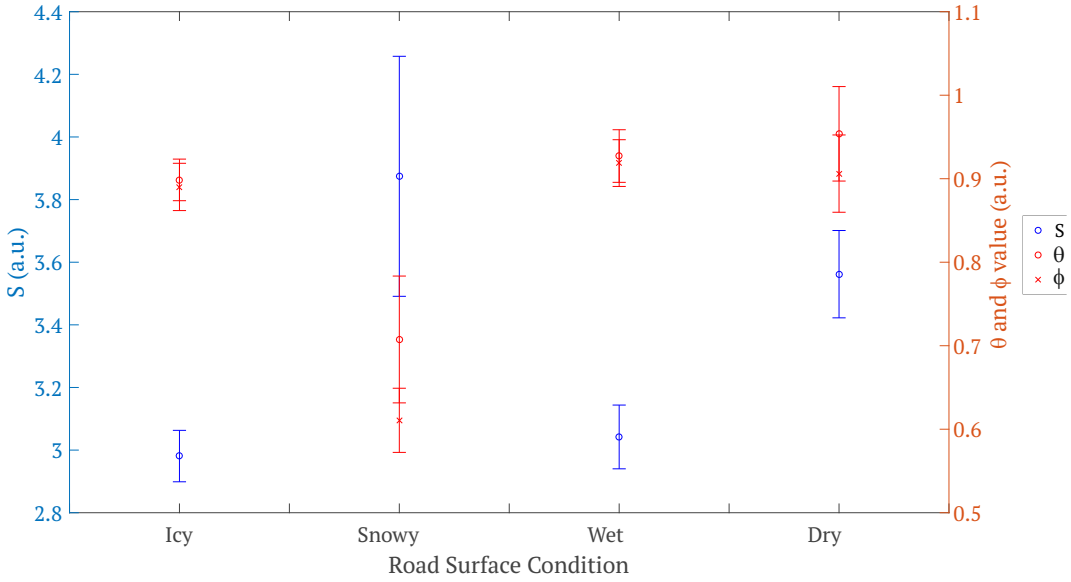

Figure 37: Errorbar plot of S parameter value for the studied surface types (left axis); Errorbar plot of θ and ϕ parameters for the studied surface types(right axis). Both plots represent values, corresponding to installation height of 600 mm.

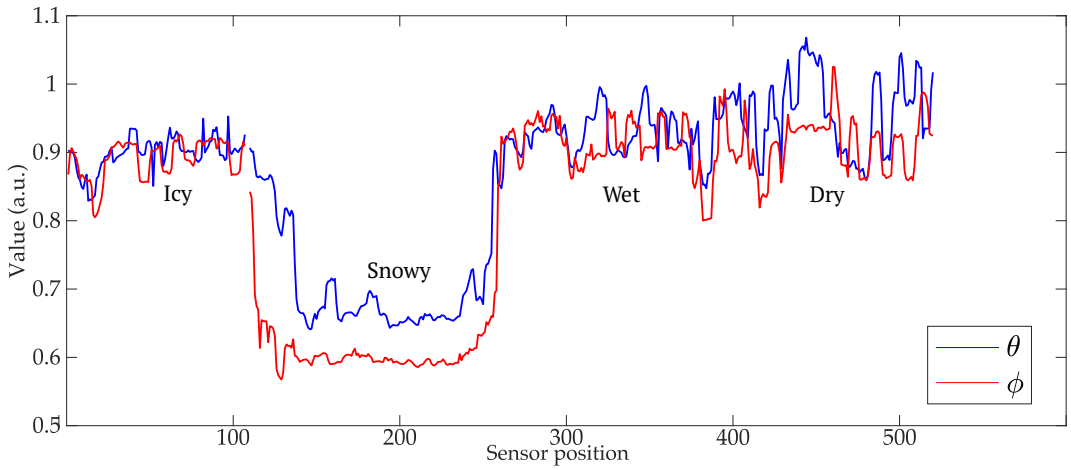

Figure 38: "Raw" values of θ and ϕ showing change of these values along the scanning direction.

change during a linear scan of a sample piece of the road surface. This plot is shown in figure 38.

For each of the surface types we got a distribution for the θ and ϕ parameters. This distribution allows us to calculate the mean value of parameters and estimate their standard deviation to facilitate prediction based upon measured data. Therefore, to get a full picture it is useful to plot θ and ϕ parameters as an error plot with errorbars representing standard deviation. These plots are shown in figures 37, 39 and 40, where errorbars show confidence boundaries of 95%. It is possible to notice that in figure 39 there is an intersection of confidence boundaries of S parameter for snowy ant wet surfaces. This can be explained by imperfections of layers on the

asphalt surface provided for that measurement.

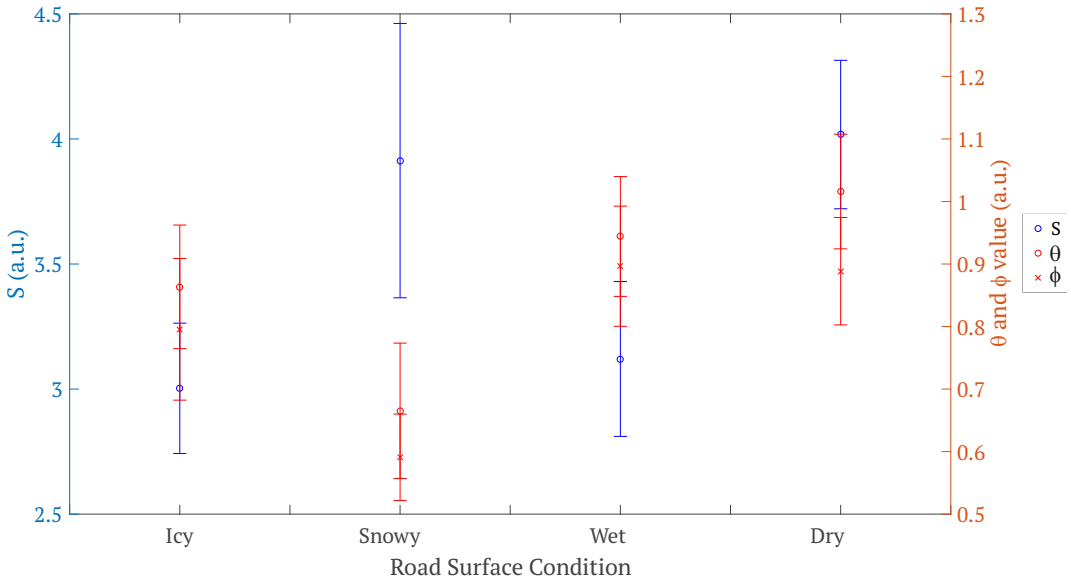

Figure 39: Errorbar plot of S parameter value for the studied surface types (left axis); Errorbar plot of θ and ϕ parameters for the studied surface types(right axis). Both plots represent values, corresponding to installation height of 400 mm.

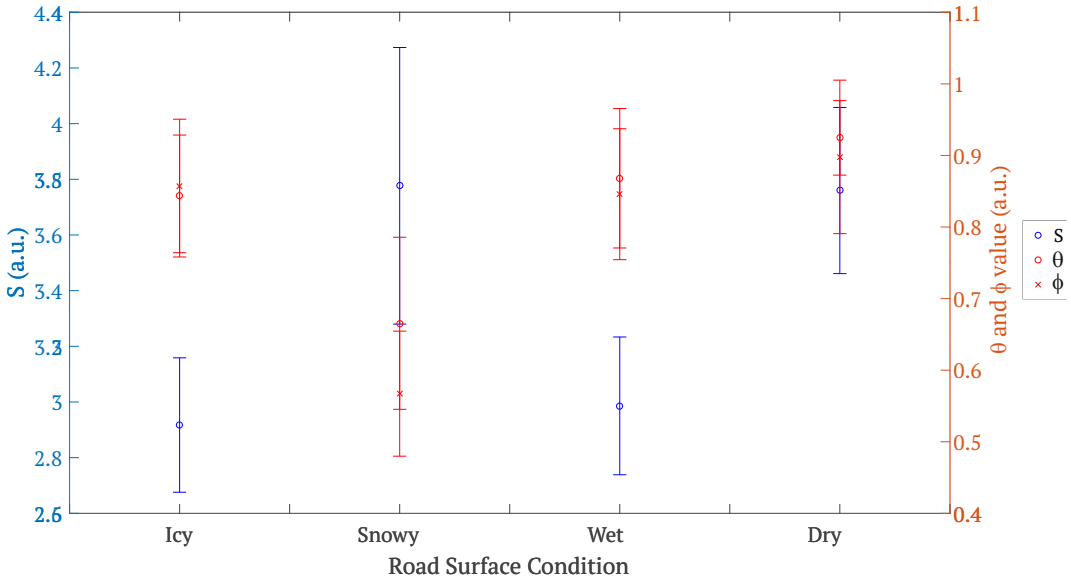

Figure 40: Errorbar plot of S parameter value for the studied surface types (left axis); Errorbar plot of θ and ϕ parameters for the studied surface types(right axis). Both plots represent values, corresponding to installation height of 500 mm.

4.3 Outcomes of Continuous Wave and Modulated Signal Measurements

It is now necessary to compare the quality of the measurement results for the CW and the modulated sensor modes of operation. This comparison is done in table 5 containing channel-specific information about the mean values and STD of both modes of operation for all the studied surfaces.

Table 5: Table of mean values and standard deviations, comparing all experimental results for the 600 mm installation height.

		$1.55\mu m$		$1.31\mu m$		$0.98\mu m$	
		Mean	STD	Mean	STD	Mean	STD
Dry	CW	0.9900	0.0077	1.0947	0.0169	1.0923	0.0167
	Mod	1.1291	0.0451	1.1854	0.0465	1.2474	0.0452
Wet	CW	0.8062	0.0097	0.9216	0.0257	0.8983	0.0119
	Mod	0.9597	0.0155	1.0366	0.0321	1.0457	0.0339
Snowy	CW	0.7938	0.0037	1.2688	0.0420	1.5890	0.0290
	Mod	0.9529	0.0136	1.3578	0.1278	1.5636	0.0719
Icy	CW	0.7584	0.0031	0.9011	0.0164	0.9108	0.0089
	Mod	0.9213	0.0239	1.0246	0.0174	1.0350	0.0274

Looking at this table, it is possible to see that the mean values are quite close to each other for both of the modes. This proves that the chosen methodology stands for different experimental conditions. However, for the the modulated signal mode the STD values are significantly larger than for the CW mode. This may be originating from imperfections of the modulation circuit affecting the signal waveform, shown in figure 24. Since demodulation decreases dramatically number of useful data points, it is possible that it affects STD as well, causing standard deviation to increase. Additionally, there can be some error in the frequency setting in the function generator, leading to some data quality loss during signal processing. This means that on current stage, it is better to rely on CW measurements.

4.4 Computer Simulations Results

The software calculates ray positions and directions. After simulation for a single value of $q_{x,0}$, it is possible to plot the actual calculated ray trajectories. Ray trajectories are shown in figure 41.

In figure 41 we can observe that the rays reflected from asphalt surface are distributed into all directions according to the Lambert's cosine law.

Performing a linear scan shows data of the same type that was gathered during the experiment. We now can plot detected ray power vs. detector position. This plot is shown in figure 42.

In figure 42 we see that for dry asphalt the reflected intensity is the same for all the three channels. This goes in argeement with the assumtion of equal reflectivity for each of the channels and geometric identity of the setups for all of these channels.

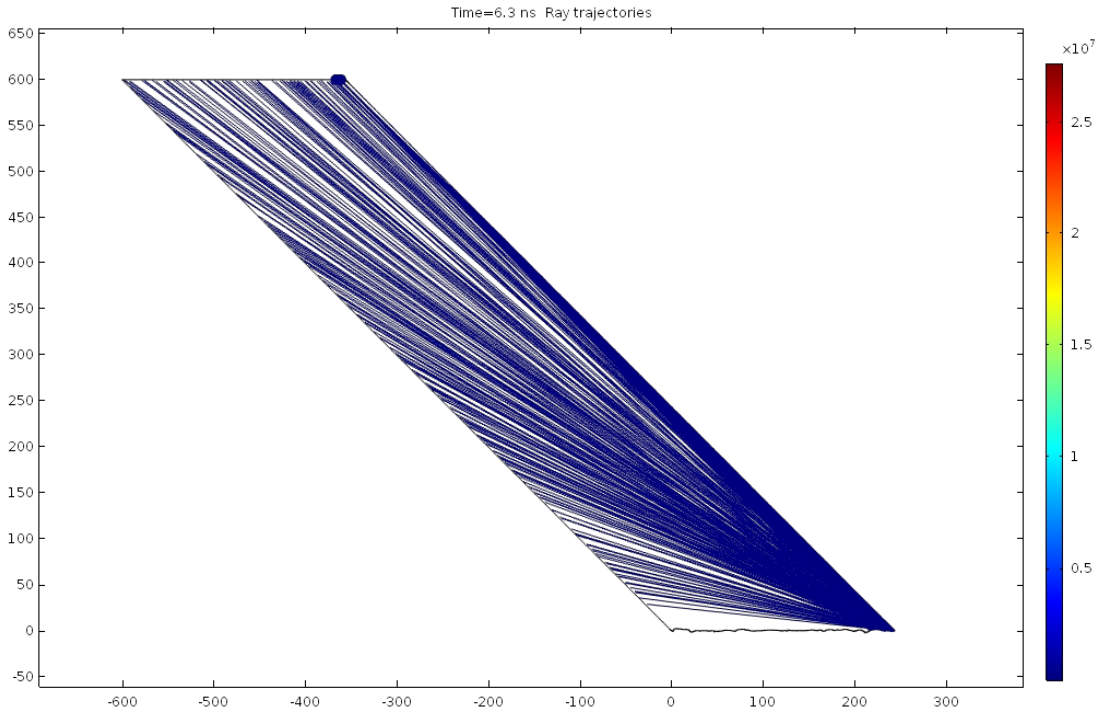

Figure 41: Ray trajectories for the last value of $q_{x,0}$ for the uncovered dry asphalt surface cross-section. Thick blue dots show detected rays.

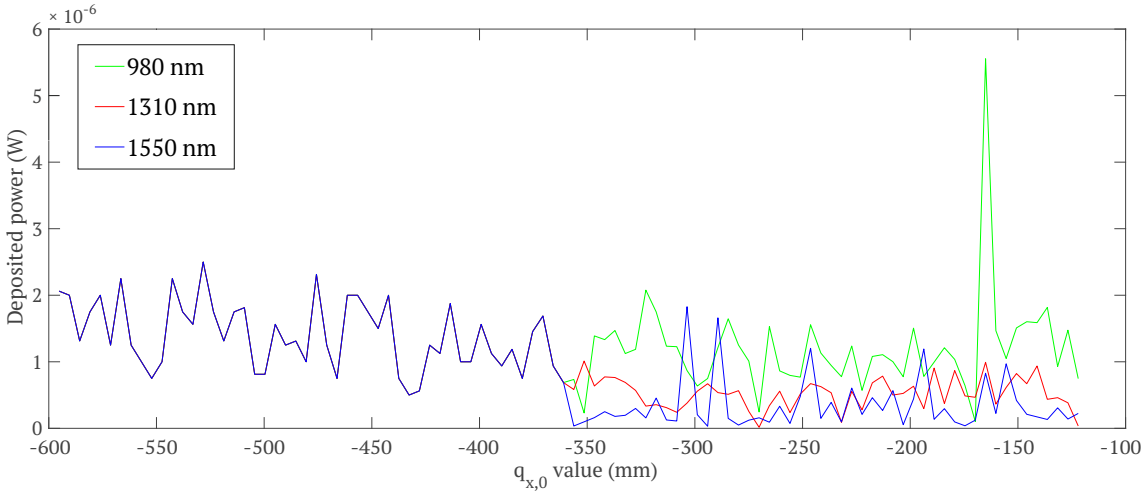

Figure 42: Plot of deposited ray power vs. relative position of the source-detector assembly to the sample surface.

For a wet surface it is seen that detected power is the largest for the 980 nm channel and the 1550 nm channel power is the least. This result supports our theoretical model. To investigate this matter further, we can calculate mean values of reflected power for our channels. Figure 43 shows the mean values of θ and ϕ parameters.

Here the reflected power distribution between channels is seen more clearly. Its value is by far the largest for the 980 nm channel, and the difference between the 1310

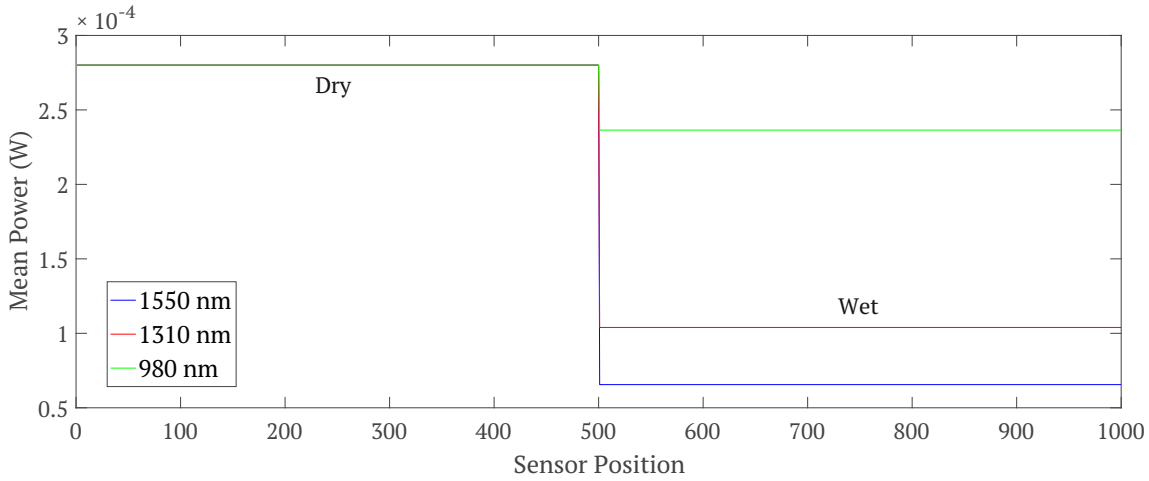

Figure 43: Plot of mean deposited ray power vs. relative position of the source-detector assembly to the sample surface.

Table 6: Mean values and STD for simulated detected ray power. Default multiplier is $\times 10^{-4}$.

	$1.55\mu m$		$1.31\mu m$		$0.98\mu m$	
	Mean	STD	Mean	STD	Mean	STD
Dry	2.801	1.025	2.801	1.025	2.801	1.025
Wet	0.656	0.855	1.039	0.452	2.364	1.516

nm and the 1550 nm channels is not that large. It is useful to estimate the quality of simulation data by also calculating STD for all of the channels and compare it to their mean value. This is done in table 6.

Large values of STD are there due to a low number of data points. Under such conditions, outliers show great influence on the calculated STD value. The time schedule and the limited computation power, unfortunately, left no opportunity for us to conduct more elaborate modelling.

As a result, computer simulations came to a good agreement with the theoretical model and the experimental results.

4.5 Discussion of Possible Improvements

Obtained measurement results and their computer simulations come in agreement with each other.

In order to make a robust and fast sensor, it is necessary to perform calculations for data processing in hardware simultaneously, not use an external computer after the raw data is gathered. In our work, we use the S parameter (sum of mean intensities) along with the θ and ϕ parameters. S can be easily acquired without pre-processing. One simply needs to turn on all of the light sources simultaneously. Calculating θ and ϕ does not also require large computational power. Division of channel voltages can be performed in digital domain simply in a digital signal processor (DSP). Moreover,

switching to digital domain as soon as possible on the signal way can significantly decrease noise coming from the circuit itself.

However, there are still drawbacks in the prototype. The most important one is unavailability to distinguish between wet and icy asphalt surfaces. Despite the great difference in absorption coefficients (see table 1) of ice for the used wavelengths, it is hard to determine the cover layer. According to equation 31, the amount of absorbed light depends also on the thickness of the cover layer. In the experiment, not mentioning real road conditions, it was not possible to provide exactly the same thicknesses of ice and water layers. Thus, considering different thicknesses, it is not possible to properly compare reflected intensities. This is the main disadvantage of the chosen method.

There is, though, a possible solution to this problem. As it was described in reference [27], the difference in reflectivity of $s-$ and $p-$ polarizations can be employed. It is stated there, that using two polarized illumination sources with the 1490 nm and the 1310 nm wavelengths can resolve ice- and water-covered surfaces. Additionally, linear polarizer is introduced before the detector. Such a setup allows to conduct measurements with pairs of s-polarized source – s-polarized detector and s-polarized source – p-polarized detector. Figure 44 shows the distribution of θ parameter for the four types of road surface coverage reprinted from [27].

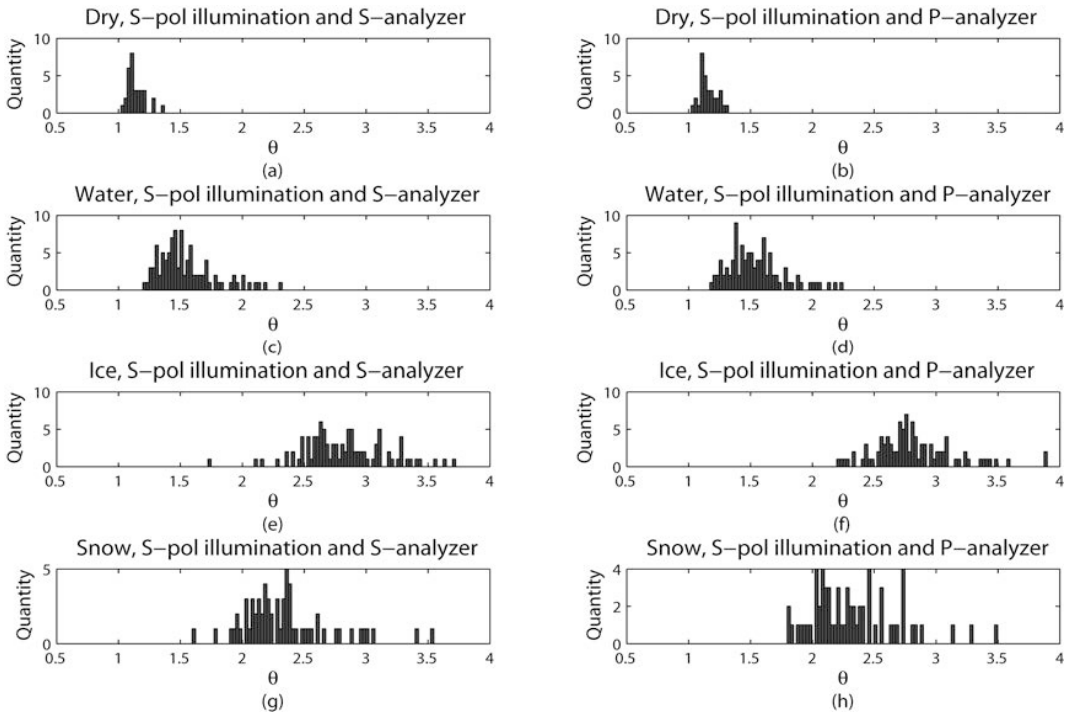

Figure 44: θ parameter distribution for the four types of road surface coverages [27].

In this representation it is easily seen that distributions for θ are not alike for wet and icy surfaces. According to this work, probability of wrong surface classification for s-analyzer was shown to be $P_{wrong} = 2.1\%$ and for a p-analyzer its value was $P_{wrong} = 0.5\%$. This is truly a good result.

The main problem with this method is the interposition of the light source and the detector. There, to get maximum intensity, the light source and the detector were positioned at the specular reflectance angle. Schematically this setup layout is depicted in figure 45.

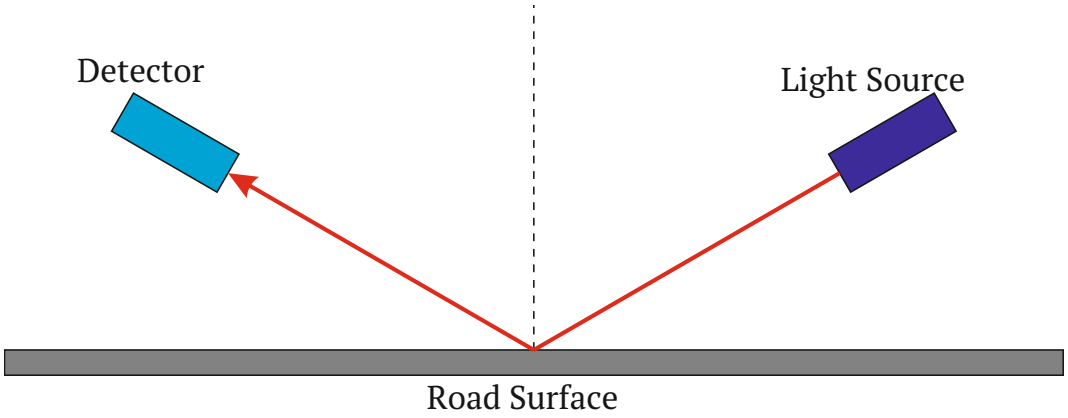

Figure 45: Source-detector interposition in experiments conducted in [27].

On one hand, getting the maximum intensity is great to obtain the best SNR, but such a layout is highly impractical in the sense of a car-mounted road sensor. It requires precise installation to provide correct s- and p- polarizations and the whole construction is sensitive to mechnical vibrations. There is a concern that after a long period of use light from the source may not reach the detector properly. Therefore, the only reasonable application of such sensor is stationary surface coverage determination. This comes in strong conflict with our idea of an affordable mobile road sensor.

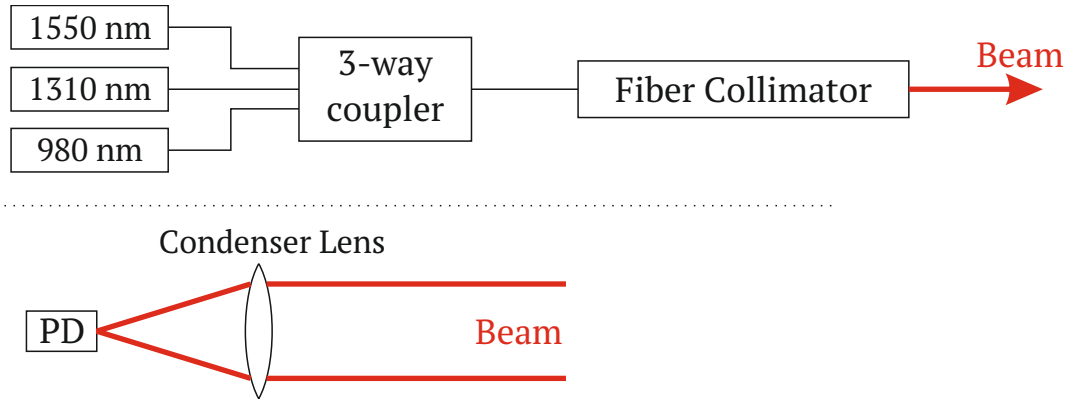

Figure 46: Principal layout of a road surface sensor with fiber collimation. PD stands for photodiode.

Another issue with our prototype is the need of averaging collected data since the light rays from the different channel sources do not have equal optical paths. To overcome this, all three light sources must be coupled through a single output window and give highly collimated beams. To accomplish that and retain robustness,

optical fiber can be used, since mirrors are very sensitive to vibrations. A principal layout of the optical parts of such a sensor is shown in figure 46.

If laser diodes are operated in short pulses, with short intervals between them, it might be possible to neglect linear movement of the sensor and thus assume car standing still during single measurement cycle. For example, if pulse is 200 ns long, car moving at 120 km/h speed will travel only 6.7 micrometers. Such a distance is supposedly small enough to assume single-point evaluation of the surface. This modification will increase the cost of the sensor, but hopefully will also increase its quality.

5 Conclusions

In this work we successfully improved optical and electronic components of a prototype and studied its ability of determining road coverge types, choosing from dry, wet, snowy and icy conditions while maintaining low cost of the previous version. Unfortunately, at the current time it is yet impossible to resolve wet asphalt from ice-covered asphalt. This comes from similar optical properties of water and ice and lack of control of the thickness of covering layer.

Computer simulations for dry and wet road surfaces showed great similarity to the experimental results. For dry asphalt, under assumption of equal reflectance for all of the used wavelengths, the profile of backreflected light is the same for all the three channels. As predicted by theory, for water-covered surface, reflected intensity is smaller. In agreement with the spectral absorption curve of water, both the experiment and the simulations showed the least reflected intensity for the 1550 nm wavelength and the maximum intensity for the 980 nm wavelength.

Particularly interesting results were obtained for the road surface covered by a thick (approximately 2 cm) layer of snow. Predictably, formed by small randomly-oriented ice crystals, snow shows diffuse reflection. In snow rays experience multiple refractions and reflections, resulting in long optical paths. Therefore, for snowy surface difference in absorption of used wavelengths is seen very clearly. Due to computational difficulty of snow particle simulation within ray tracing approach, it was impossible to implement a computer simulation showing additional proof of correct explanation for snow scattering and absorbtion origins.

As a future prospect, it is possible to make some improvements in the sensor. First, it is possible to rebuild the electric circuit to improve the quality of signal modulation. This upgrade will require replacement of the laser driving IC with a capability of external triggering and installation of a built-in signal generator. It is also useful to implement a built-in DAQ system. This will reduce size of the prototype and give a possibility to communicate with other systems.

Upgrades in the optical parts mentioned in chapter 4 will most certainly severely affect the final cost of the device. Arguably, they could improve its quality and broaden the ability to detect precisely different kinds of surfaces. This can be determined only through further experimental work and simulations.

Also, it may be possible to implement a system providing measurement of water or ice thickness. Based on this data, it will be possible to finally distinguish between water and ice coverage of road surface.

References

[1] H. Heinijoki, "Influence of the type and condition of tires and drivers' perception of road conditions on driving speed," *FinnRA reports 19/1994*, 1994.

[2] C.-G. Wallman, "Driver behavious on winter roads: A driving simulator study," in *Xth PIARC International Winter Road Congress*, vol. 3, 1998.

[3] B. Schmidt, *Friktionsmålinger: sammenlignende målinger mellem ROAR og Stradograf*. Vejdirektoratet, Vejteknisk Institut, 1999.

[4] S. Li and T. Kawabe, "Slip suppression of electric vehicles using sliding mode control method," 2013.

[5] F. Gustafsson, "Slip-based tire-road friction estimation," *Automatica*, vol. 33, no. 6, pp. 1087–1099, 1997.

[6] G. Erdogan, L. Alexander, and R. Rajamani, "Estimation of tire-road friction coefficient using a novel wireless piezoelectric tire sensor," *Sensors Journal, IEEE*, vol. 11, no. 2, pp. 267–279, 2011.

[7] R. Matsuzaki and A. Todoroki, "Wireless strain monitoring of tires using electrical capacitance changes with an oscillating circuit," *Sensors and Actuators A: Physical*, vol. 119, no. 2, pp. 323–331, 2005.

[8] A. J. Tuononen, "Laser triangulation to measure the carcass deflections of a rolling tire," *Measurement Science and Technology*, vol. 22, no. 12, p. 125304, 2011.

[9] T. Dieckmann, "Assessment of road grip by way of measured wheel variables," in *XXIV FISITA CONGRESS, 7-11 JUNE 1992, LONDON. HELD AT THE AUTOMOTIVE TECHNOLOGY SERVICING SOCIETY. TECHNICAL PAPERS. SAFETY, THE VEHICLE AND THE ROAD. VOLUME 2 (IMECHE NO C389/349 AND FISITA NO 925227)*, 1992.

[10] A. Pohl, R. Steindl, and L. Reindl, "The "intelligent tire" utilizing passive saw sensors measurement of tire friction," *Instrumentation and Measurement, IEEE Transactions on*, vol. 48, no. 6, pp. 1041–1046, 1999.

[11] A. J. Niskanen and A. J. Tuononen, "Accelerometer tyre to estimate the aquaplaning state of the tyre-road contact," in *2015 IEEE Intelligent Vehicles Symposium (IV)*, pp. 343–348, IEEE, 2015.

[12] M. J. Matilainen and A. J. Tuononen, "Tire friction potential estimation from measured tie rod forces," in *Intelligent Vehicles Symposium (IV), 2011 IEEE*, pp. 320–325, IEEE, 2011.

[13] D. Gailius and S. Jačenas, "Ice detection on a road by analyzing tire to road friction ultrasonic noise," *Ultragarsas*, vol. 62, no. 2, pp. 17–20, 2007.

[14] R. Finkele, "Detection of ice layers on road surfaces using a polarimetric millimetre wave sensor at 76 ghz," *Electronics Letters*, vol. 33, no. 13, pp. 1153–1154, 1997.

[15] J. Casselgren, M. Sjödahl, and J. LeBlanc, "Angular spectral response from covered asphalt," *Applied optics*, vol. 46, no. 20, pp. 4277–4288, 2007.

[16] "Teconer®rcm411 sensor datasheet." http://www.teconer.fi/downloads/RCM_Datasheet_en.pdf. Accessed: 2016-10-01.

[17] "Lufft®marwis sensor website." http://www.lufft-marwis.de/en_US/features. Accessed: 2016-10-01.

[18] M. Herold, D. Roberts, O. Smadi, and V. Noronha, "Road condition mapping with hyperspectral remote sensing," in *Proceedings of the 2004 AVIRIS workshop, March*, 2004.

[19] A. I. Lvovsky, "Fresnel equations," 2013.

[20] M. Kaivola, "Optical physics, light and matter." 2014.

[21] J. C. Stover, *Optical scattering: measurement and analysis*, vol. 2. SPIE optical engineering press Bellingham, 1995.

[22] S. Kedenburg, M. Vieweg, T. Gissibl, and H. Giessen, "Linear refractive index and absorption measurements of nonlinear optical liquids in the visible and near-infrared spectral region," *Optical Materials Express*, vol. 2, no. 11, pp. 1588–1611, 2012.

[23] S. G. Warren, "Optical constants of ice from the ultraviolet to the microwave," *Applied optics*, vol. 23, no. 8, pp. 1206–1225, 1984.

[24] C. R. Longwell, R. F. Flint, and J. E. Sanders, *Physical geology*. Wiley, 1969.

[25] S. W. Smith *et al.*, "The scientist and engineer's guide to digital signal processing," 1997.

[26] L. Orozco, "Synchronous detectors facilitate precision, low-level measurements," *Analog Dialogue*, vol. 48, no. 11, 2014.

[27] J. Casselgren, *Road surface classification using near infrared spectroscopy*. PhD thesis, Luleå University of Technology, 2007.